Stereoisomeric Mixture of a Multigram-Synthesized Helicene Assembles Swiftly into Hierarchical Ribbons via Supramolecular Sheets

Nathaniel J. Schuster[a+], Rachael K. Mow[b+], Hao Lyu[a], Max Schrock[b], Ruiheng Wu[a], Yilei Wu[a], Song Zhang[a], Xi Jiang[c], Zhenan Bao[a*]

[+]These authors contributed equally to the work

[a]Department of Chemical Engineering, Stanford University, Stanford, CA 94305, USA

[b]Department of Chemistry, Stanford University, Stanford, CA 94305, USA

[c]Materials Sciences Division, Lawrence Berkeley National Laboratory, Berkeley, CA 94720, USA

Email address of the corresponding author: zbao@stanford.edu

Table of Contents

I. Figures Referenced in the Article

Supplementary Figure S1. Picture of 10 grams of **H-N[5]HDI** following isolation from its Taüber reaction mixture. A United States one cent piece is included for scale.

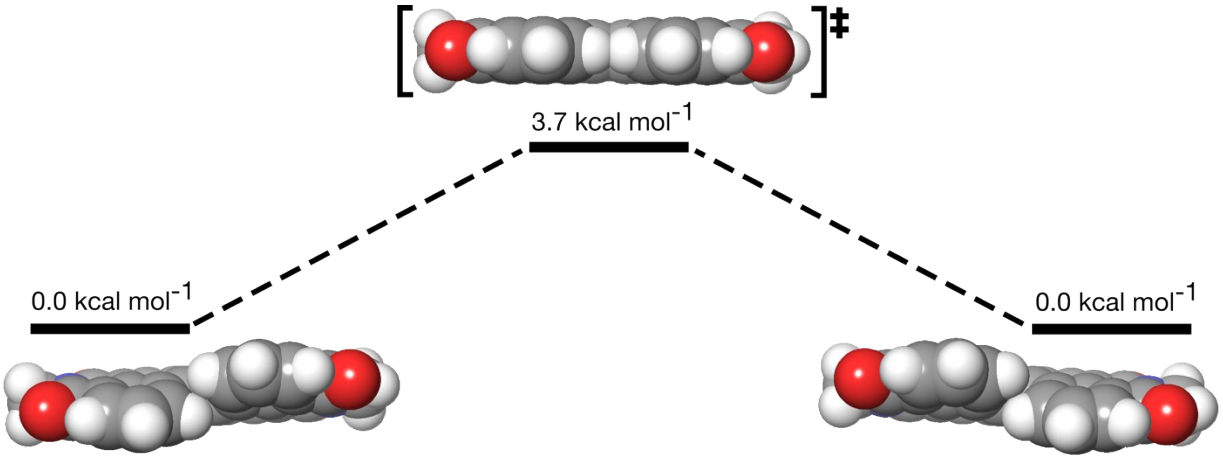

Supplementary Figure S2. In solution at room temperature, **H-N[5]HDI** rapidly isomerizes between its left- and right-handed helical geometries. Here, the minima and transition-state geometries were calculated in the gas phase at the B3LYP-D3/6-31G** level of DFT, and the energies correspond to $\Delta G_{298\ K}$ calculated at the B3LYP-D3/6-31G** level of DFT. The alkyl chains were truncated to methyl groups to simplify the calculations.

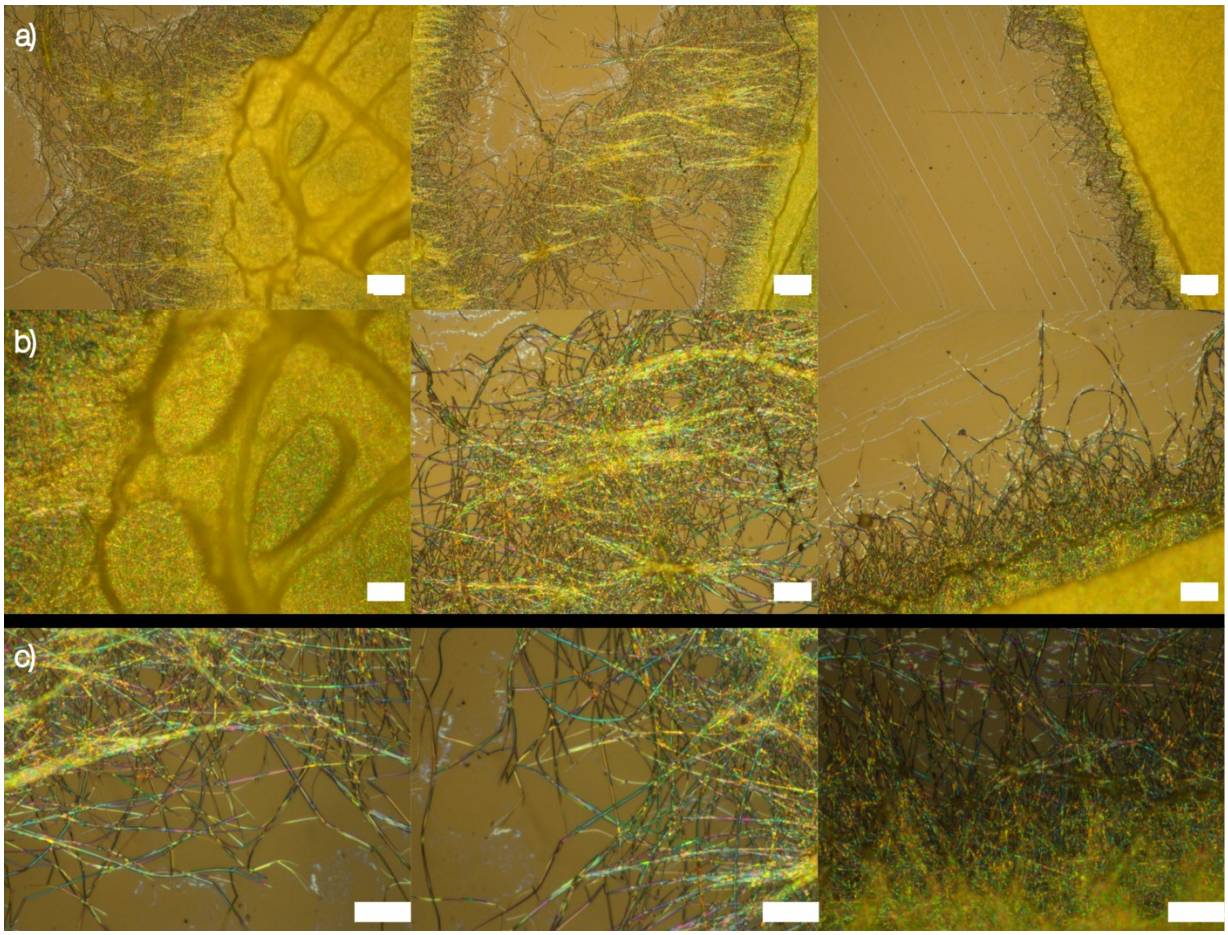

Supplementary Figure S3. Optical microscopy images of the peripheries of drop-cast ribbons of **H-N[5]HDI** under polarized light, where the polycrystalline entangled fibrillar substructure is evident. Three different ribbons at (**a**) 20× magnification and (**b**) 50× magnification. (**c**) Additional fibers imaged at 100× magnification.

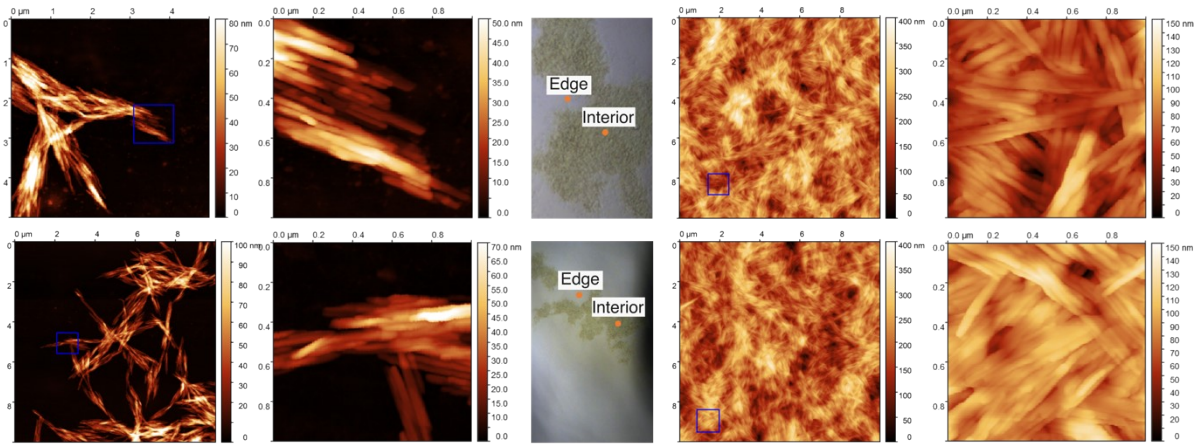

Supplementary Figure S4. AFM images of proto-fibers formed via filament bundling on the edge (left four images) and interior (right four images) of ultrasonicated ribbons. Each pair of images includes a larger area measurement (left) and a selected area (outlined in blue) that was measured at higher resolution (right).

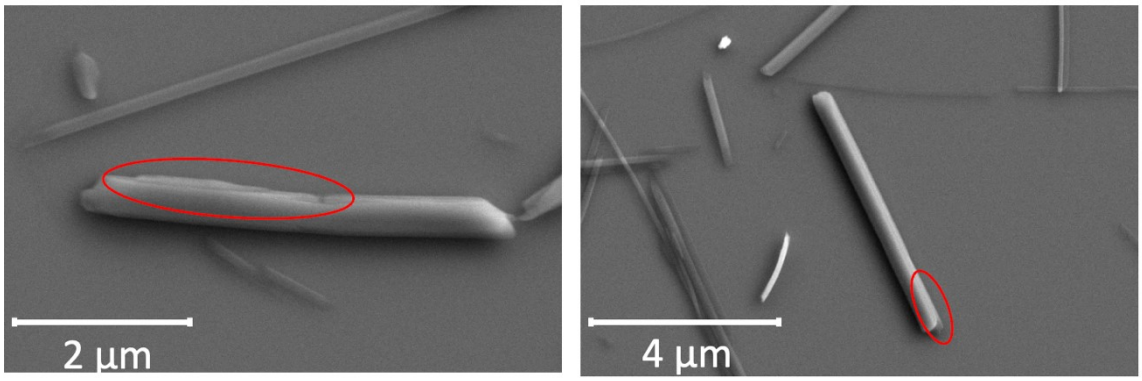

Supplementary Figure S5. Sheets glimpsed at the edges of fractured filaments of **H-N[5]HDI**, as observed by SEM.

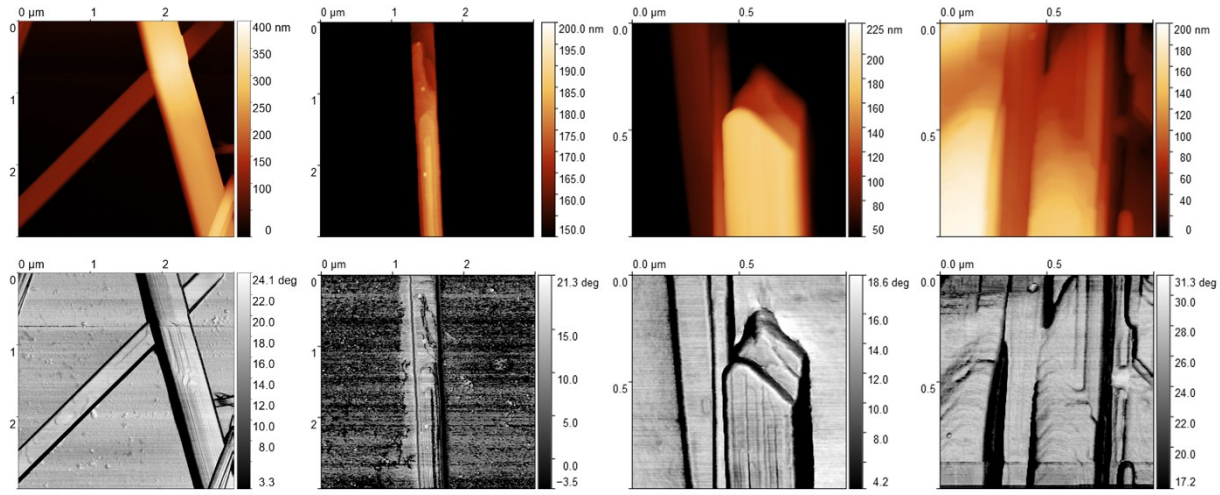

Supplementary Figure S6. Additional AFM images (top) and their phase-contrast counterparts (bottom) showing terracing on filaments after exfoliation. These terraces underscore that a sheet-based substructure constitutes the filaments of **H-N[5]HDI**.

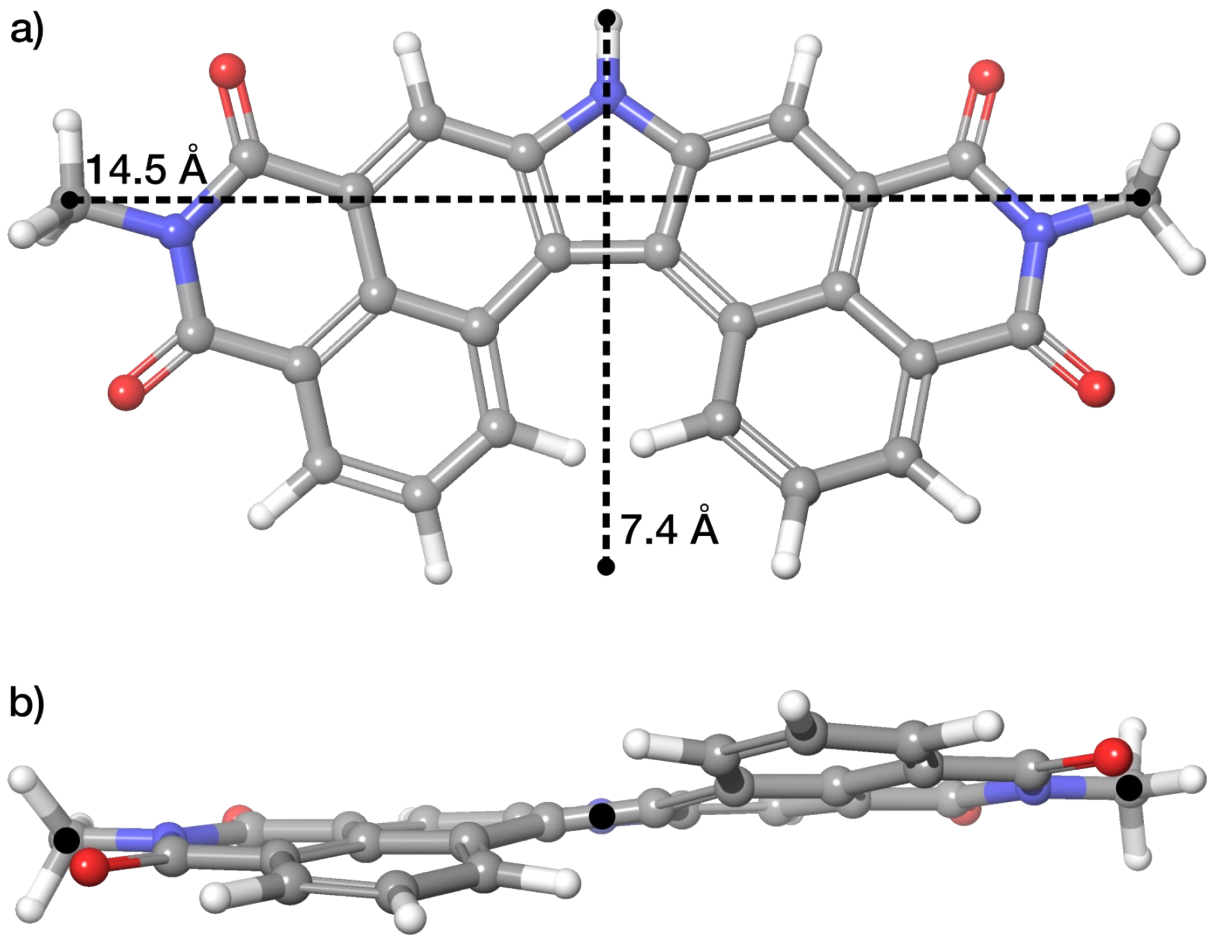

Supplementary Figure S7. (**a**) The width (7.4 Å) and α-carbon-to-α-carbon length (14.5 Å) of the DFT-optimized structure of **H-N[5]HDI** (at the B3LYP-D3/6-31G** level of theory). The alkyl chains were truncated to methyl groups to simplify the calculation. (**b**) The same model from another perspective.

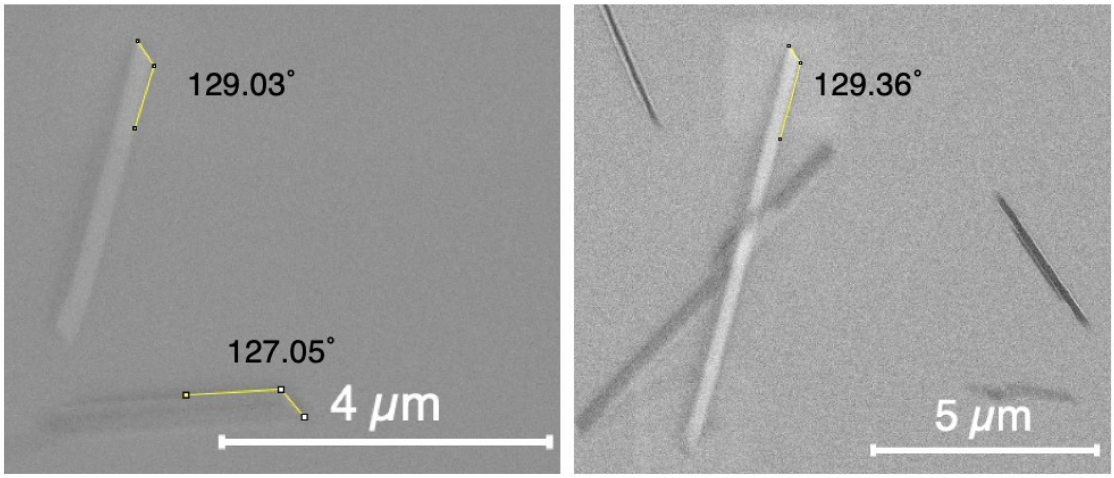

Supplementary Figure S8. As observed by SEM, the edge-to-end angle of the facets of intact filaments of **H-N[5]HDI** matches the *β* angles of the packing models proposed from GIWAXS: 125° and 126° for the *C*2 and *Cc* unit cells, respectively.

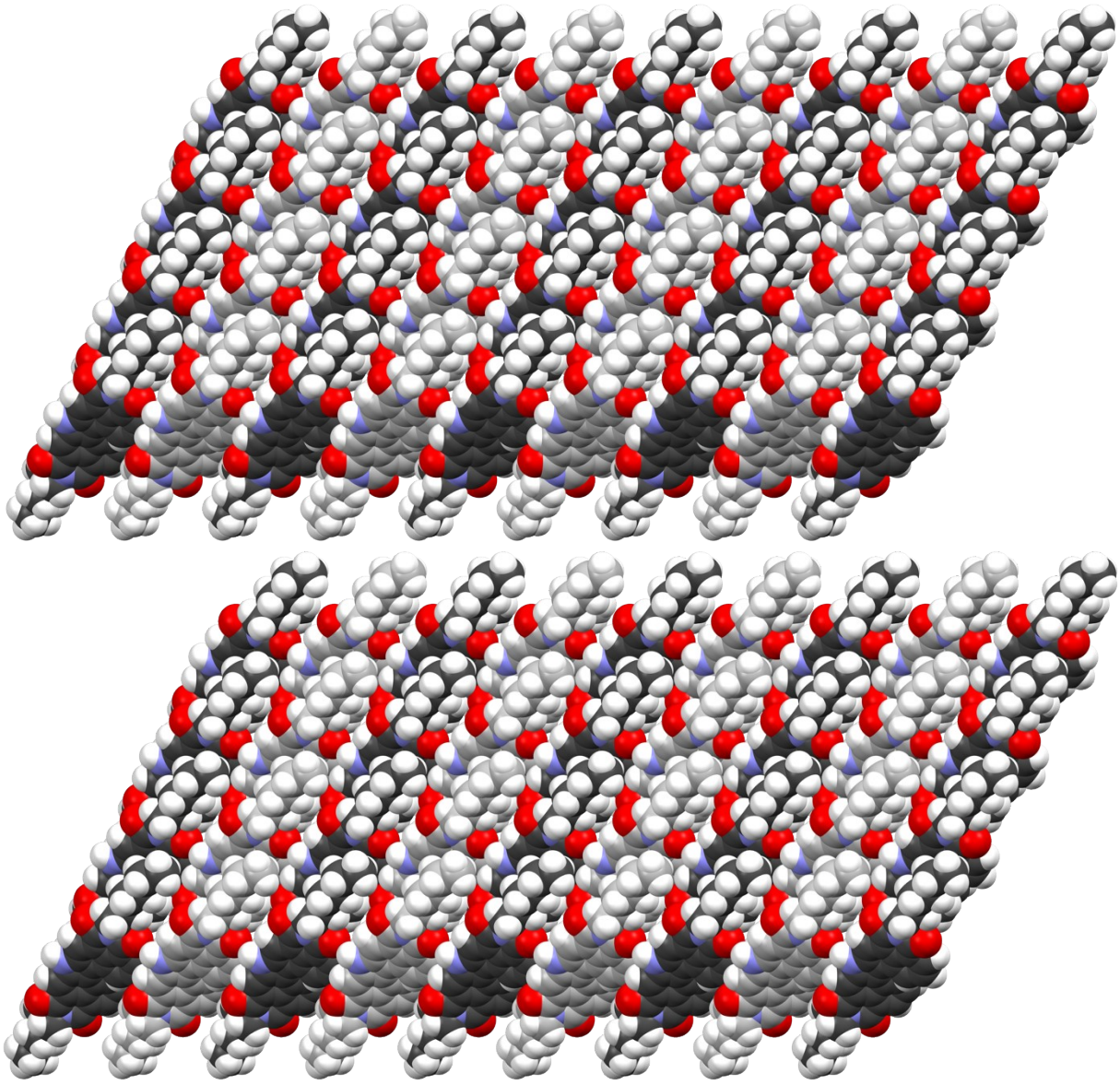

Supplementary Figure S9. A single sheet of **H-N[5]HDI** within the proposed *C*2 (top) and *Cc* (bottom) packing models. In the sheets above, every molecule has an (*R,S*) configuration and left-handed helical geometry. Here, the molecular rows assembled through CH–π interactions are emphasized, with the carbon atoms of every other row colored in different shades of grey. Contrast with Supplementary Figure S10, which is an alternative rendering of the same sheets.

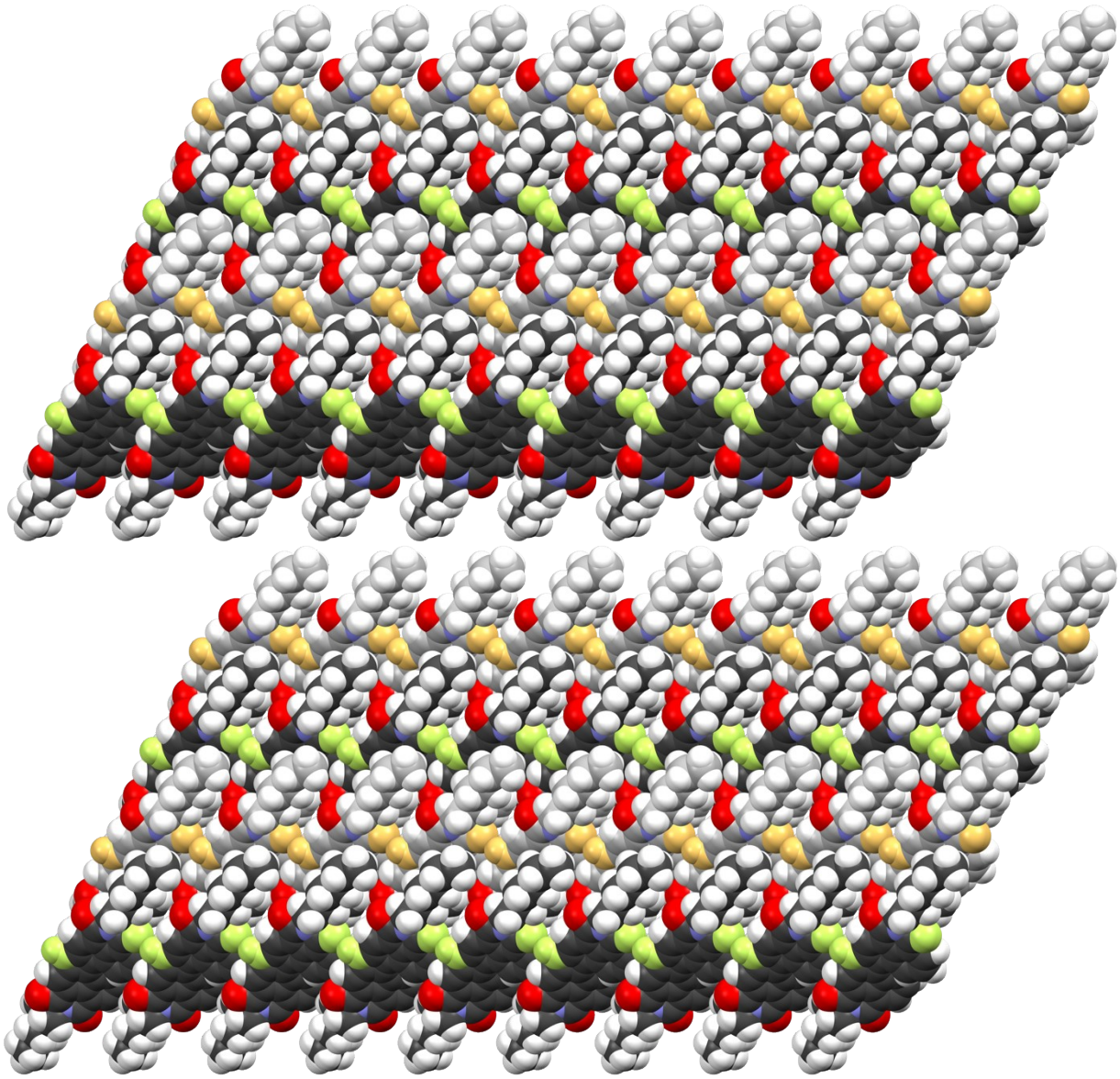

Supplementary Figure S10. A single sheet of **H-N[5]HDI** within the proposed *C*2 (top) and *Cc* (bottom) packing models. In the sheets above, every molecule has an (*R,S*) configuration and left-handed helical geometry. Here, the molecular rows assembled through weak hydrogen bonding are emphasized, with the carbon atoms of every other row colored in different shades of grey. Additionally, the hydrogen bond donors (the pyrrolic N–H) and acceptors (a carbonyl O) are highlighted in bright green and orange. Contrast with Supplementary Figure S9, which is an alternative rendering of the same sheets.

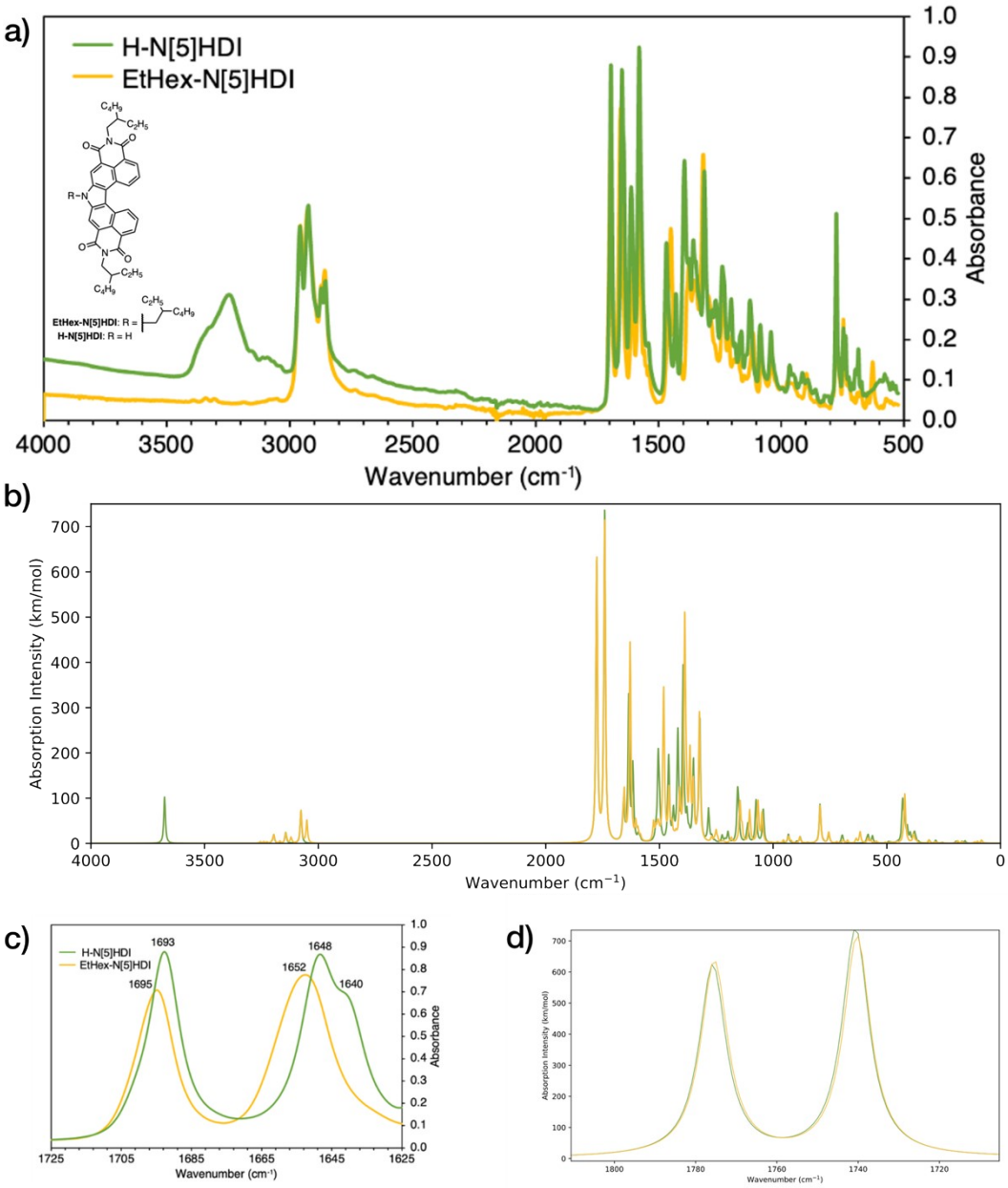

Supplementary Figure S11. (**a**) Experimental FTIR spectra of **H-N[5]HDI** (supramolecular ribbon) and **EtHex-N[5]HDI** (powder). (**b**) From DFT (B3LYP-D3/6-31G**), the predicted vibrational spectra of **H-N[5]HDI** and **EtHex-N[5]HDI** in the gas phase (simulated in the Plot Spectrum feature of Maestro by Schrödinger: Lorentzian line shapes, scale factors of 1.0, and half-bandwidths of 4). To expedite these calculations, the alkyl chains were truncated to methyl groups. (**c**) The absorbances corresponding to the carbonyl stretches within the experimental IR spectra of **H-N[5]HDI** and **EtHex-N[5]HDI**. Note the probable influence of weak hydrogen bonding on the lower wavenumber peak of **H-N[5]HDI**: a shoulder feature at ~1640 cm^{-1}, which disappears upon substitution of the hydrogen-bond donor (the pyrrolic nitrogen atom) with an ethylhexyl chain (i.e., **EtHex-N[5]HDI**). This shoulder feature is also absent in the predicted spectrum of **H-N[5]HDI** (**d**), as the DFT calculation was executed in the gas-phase and therefore does not reflect the influence of intermolecular interactions (e.g., hydrogen bonding).

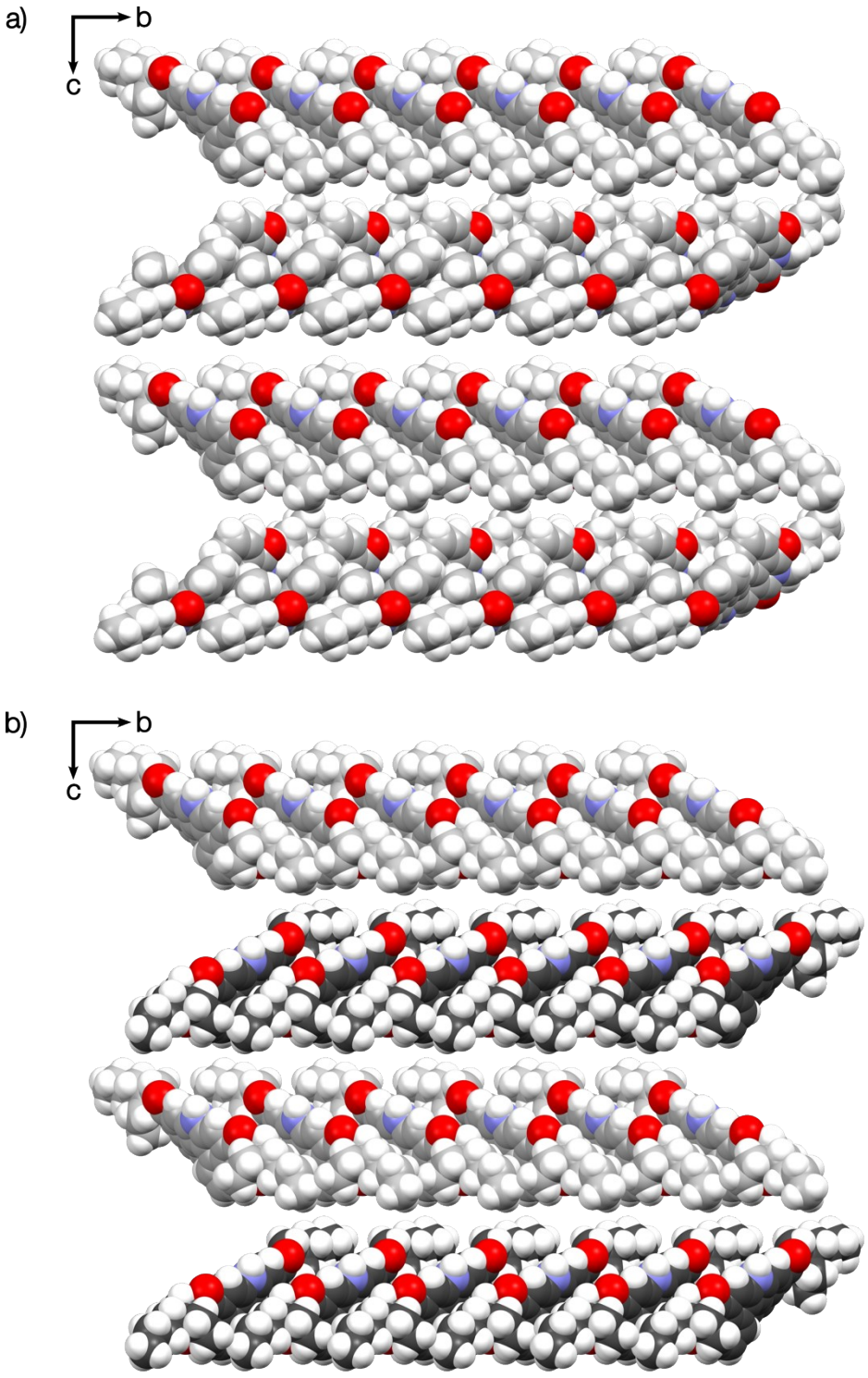

Supplementary Figure S12. Four stacked sheets of **H-N[5]HDI** within the proposed *C*2 (**a**) and *Cc* (**b**) packing models. Every sheet is composed of helicenes of exclusively one handedness; however, whereas all sheets in the *C*2 structure have the same handedness (in the case above, all left-handed), the sheets in the *Cc* structure alternate in the handedness of their helicenes. The carbon atoms of left-handed helicenes are rendered in light grey, whereas the carbon atoms of right-handed helicenes are rendered in dark grey. See Supplementary Figure S13 for another perspective.

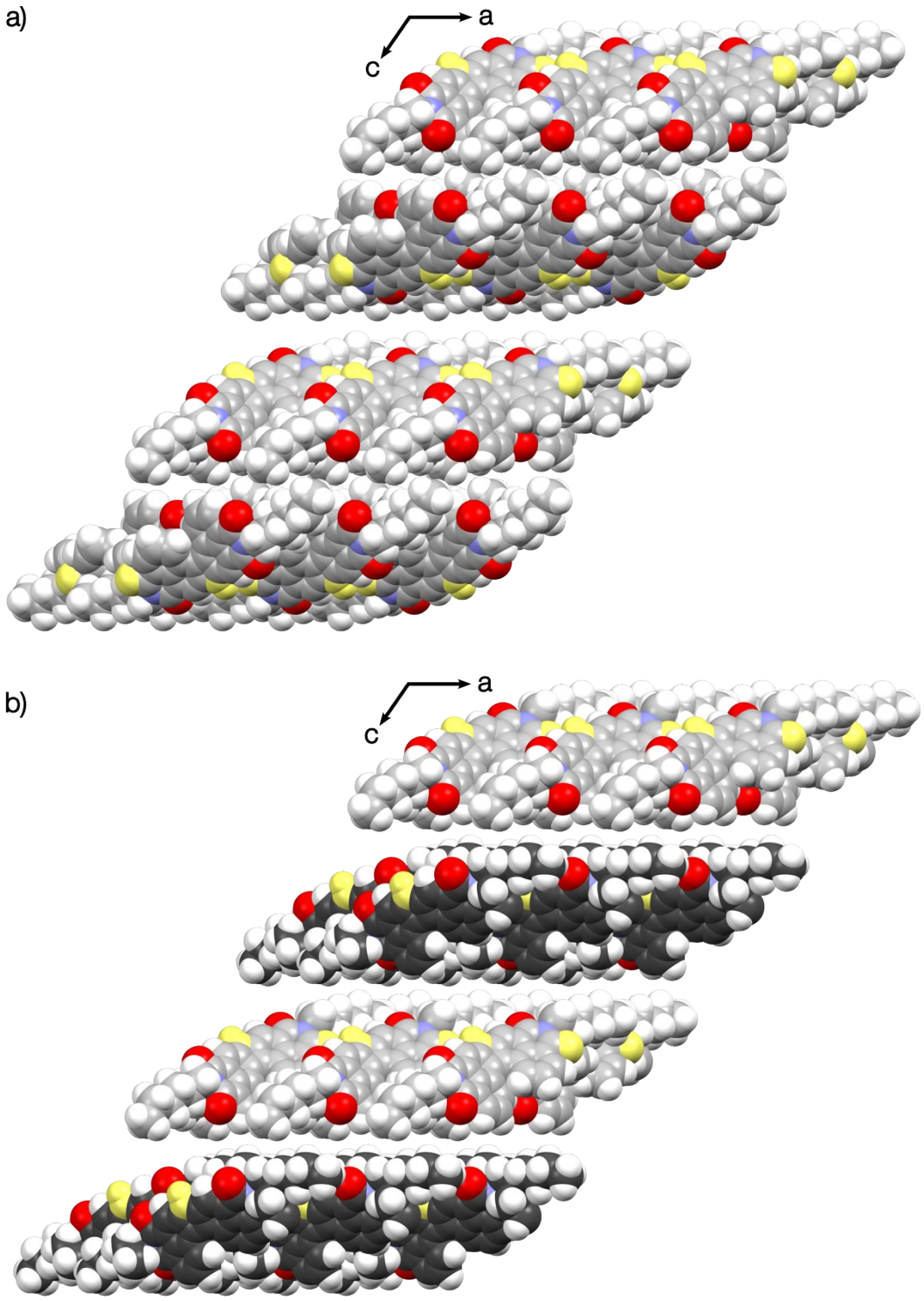

Supplementary Figure S13. Four stacked sheets of **H-N[5]HDI** within the proposed *C*2 (**a**) and *Cc* (**b**) packing models. Every sheet is composed of helicenes of exclusively one handedness; however, whereas all sheets in the *C*2 structure have the same handedness (in the case above, all left-handed), the sheets in the *Cc* structure alternate in the handedness of their helicenes. The carbon atoms of left-handed helicenes are rendered in light grey, whereas the carbon atoms of right-handed helicenes are rendered in dark grey. Atoms participating in weak hydrogen bonding are highlighted. See Supplementary Figure S12 for another perspective.

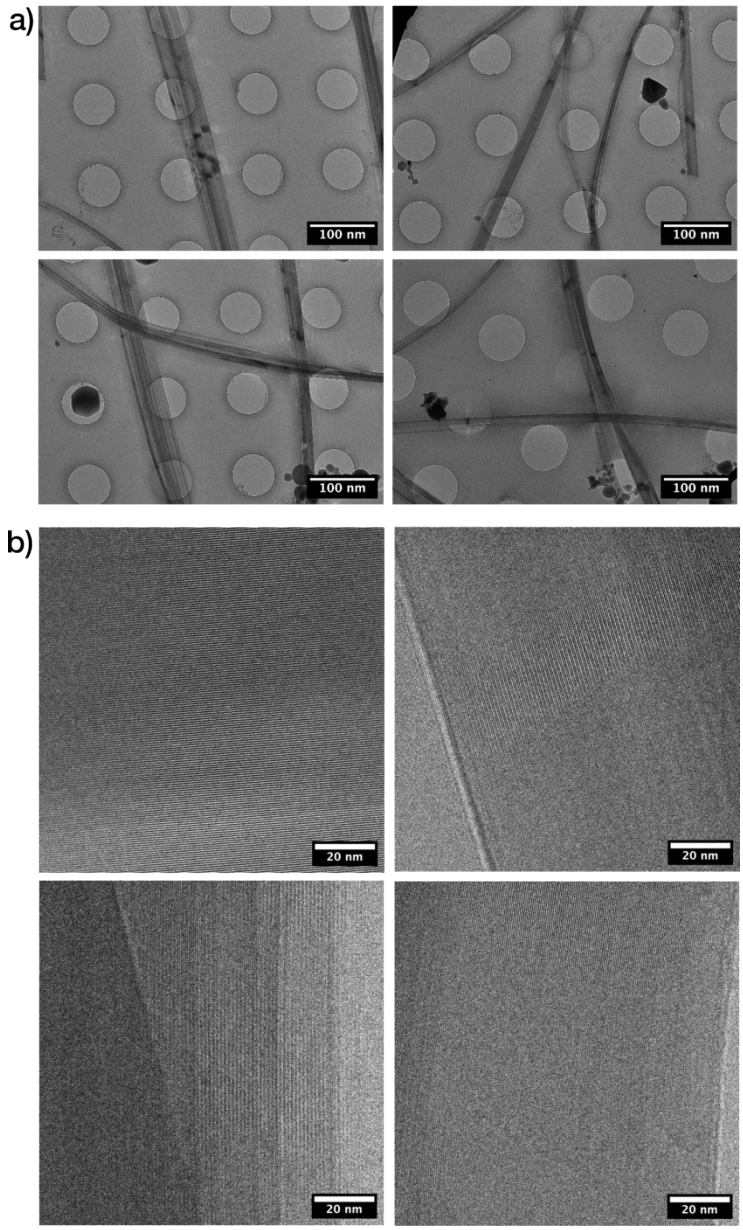

Supplementary Figure S14. Cryo-TEM images of filaments cast from mixtures of "as-grown" ribbons at (**a**) lower magnification and (**b**) higher magnification, where well-ordered rows of **H-N[5]HDI** are discernible.

II. General Experimental Information

Synthesis: All reactions were conducted in the designated oven-dried glassware. Schlenk flasks were evacuated and backfilled with nitrogen three times prior to use. Anhydrous Sure-Sealed 1-methyl-2-pyrrolidone (NMP) was used as purchased from Sigma-Aldrich. *N*,*N*-dimethylformamide (DMF) was dispensed from a Glass Contour solvent system consisting of a Schlenk manifold with purification columns packed with activated alumina and supported copper catalyst. The DMF for the solvent system was purchased anhydrous and Sure-Sealed from Sigma-Aldrich. Sulfuric acid (ACS Grade), hydrochloric acid (Certified ACS Plus), reagent alcohol (by volume, 90% ethanol, 5% methanol, and 5% isopropanol), acetonitrile (Certified ACS), hexanes (Certified ACS), dichloromethane (DCM; Certified ACS), and ethyl acetate (EtOAc; Certified ACS) were used as purchased from Fisher Chemical. Sodium nitrate (ReagentPlus, ≥99.0%), tin(II) chloride (reagent grade, 98%), *p*-toluenesulfonic acid monohydrate (*p*TsOH•H_2O; ReagentPlus, ≥98%), and 1,8-naphthalic anhydride were used as purchased from Sigma-Aldrich. 2-Ethylhexylamine (>98.0%), benzoic acid (>99.0%), 1-bromo-2-ethylhexane (>97.0%), and 1,8-diazabicyclo[5.4.0]-7-undecene (DBU; >98.0%) were used as purchased from Tokyo Chemical Industry Company. Copper(I) thiophene-2-carboxylate (CuTC; 98%) was used as purchased from Oakwood Chemical. 4-Bromo-1,8-naphthalic anhydride (96%) was used as purchased from BLDpharm. The procedure for the synthesis of **2** was adapted from Zhang *et al*[1].

NMR Spectroscopy: ^{1}H-NMR spectra were recorded on a Bruker 400 MHz spectrometer. ^{13}C-NMR spectra were recorded on a Bruker 101 MHz spectrometer with complete proton decoupling. Chemical shifts for protons are reported in parts per million (ppm) downfield from tetramethylsilane (TMS) and were referenced to residual protium in the NMR solvent (DMSO-d_6, δ 2.50; $CDCl_3$, δ 7.26; $C_2D_2Cl_4$, δ 6.00)[2,3]. Chemical shifts for carbon are reported in ppm downfield from TMS and were referenced to the carbon resonances of the NMR solvent (DMSO-d_6, δ 39.53; $CDCl_3$, δ 77.06; $C_2D_2Cl_4$, δ 73.78)[2,3]. ^{1}H-NMR data are represented as follows: chemical shift, multiplicity (s = singlet, bs = broad singlet, d = doublet, bd = broad doublet, t = triplet, bt = broad triplet, dd = doublet of doublets, m = multiplet, bm = broad multiplet), coupling constants in Hz, and integration. The spectra were recorded at 298 K, except for **H-N[5]HDI**; its spectra were recorded at 373 K. Peaks in the alkyl regions of compounds **4**, **H-N[5]HDI**, and **EtHex-N[5]HDI** have skewed integration due to overlap with the peak from water, and of compound **5** due to unresolved contaminants.

High-Resolution Mass Spectrometry (HRMS): HRMS was conducted by electrospray ionization mass spectrometry (ESI-MS) using a Waters Q-TOF Ultima spectrometer at the School of Chemical Sciences Mass Spectrometry Laboratory (MSL) at the University of Illinois Urbana-Champaign.

Preparation of the Supramolecular Assembly: Ribbons of **H-N[5]HDI** were prepared by first dispersing ≥500 mg of **H-N[5]HDI** in DCM. The resultant fine suspension was dried onto silica by rotary evaporation. If the loaded silica was clumpy following drying, additional DCM and silica were added to the mixture and then dried by rotary evaporation. These dispersals and dryings were repeated until the loaded silica flowed freely. The loaded silica was added to a 25-gram RediSep cartridge from Teledyne Isco and extracted as follows: The solution of **H-N[5]HDI** in 10%

EtOAc/DCM (v/v) was passed through a 24-gram Redisep Silver normal-phase silica flash column from Teledyne Isco (40–60 μm particle size, column bed of 2.26-cm diameter and 10.82-cm length) on a Teledyne Isco Combiflash Rf200 auto-column (see Supplementary Figure S48 in Section IX for additional details) and collected in 25-mL fractions in 18×150 mm test tubes. Certified ACS hexanes, DCM, and EtOAc from Fisher Chemical were used as the eluents. The eluate of **H-N[5]HDI** was not disturbed for at least 10 min following elution from the column. The more concentrated fractions formed ribbons within seconds, and a maximum ribbon density was achieved within 10 min. The less concentrated fractions also formed ribbons but required longer growth periods. For optical microscopy and SEM, test tubes of ribbons of **H-N[5]HDI** were decanted, backfilled with DCM to disperse the ribbons, and then ribbons were drawn-up and drop-cast by glass pipet onto glass slides or bare silicon wafers. From the test tube with the greatest yield of ribbons, other samples were prepared by diluting 1 mL of the mixture with 9 mL of hexanes in a 20-mL scintillation vial. While cooled externally by an ice bath, this diluted mixture was tip-ultrasonicated by a Cole Parmer 750 W ultrasonicator for 20 min at 20% amplitude, 1 s pulse intervals (see Supplementary Figure S48c). The resultant fine ribbons were suitable for AFM and high-resolution TEM analyses (see Supplementary Figure S4, but note that the exfoliated filaments in Supplementary Figures S6, S34, and S37, in contrast, were prepared by rinsing drop-cast, “as-grown” ribbons with DCM on a glass slide).

Optical Microscopy: Optical microscope images of ribbons of **H-N[5]HDI** drop-cast on glass slides were taken on a Nikon Eclipse LV100N POL Microscope. The thick cores of the ribbons were difficult to image; however, the highly entangled fibrillar substructure was easily observed at the edges of the ribbons. Birefringence within the fibers when observed by polarized light underscored the polycrystalline nature of the ribbons.

Scanning Electron Microscopy (SEM): SEM images of ribbons of **H-N[5]HDI** drop-cast on bare silicon were taken on an FEI Magellan 400 XHR Scanning Electron Microscope at Stanford Nano Shared Facilities (SNSF). The cores of the ribbons were imaged by SEM, as well as discrete filaments at the edges of the ribbons. The edge-to-end angles of the facets of intact filaments (see Supplementary Figure S8) were measured using the ImageJ 1.54g image processing software[4].

Atomic Force Microscopy (AFM): AFM images of Filament 1 were taken in Standard Tapping mode on a Bruker Dimension Icon AFM with a NanoScope5 controller. An AC300TS probe (Oxford Instruments, with a nominal tip radius of 7 nm, resonance frequency of 150 kHz, and spring constant of 9 N/m) was used. The scan resolution was set to 128x256 pixels with a scan rate of 0.8 Hz. AFM images of Filaments 2–6 were taken in Quantitative NanoMechanical Measurement mode on a Bruker Dimension Icon AFM with a NanoScope5 controller. A Self-Adjust Air probe (MikroMasch, with a nominal tip radius of 2 nm, resonance frequency of 70 kHz, and spring constant of 0.4 N/m) was used. The scan resolution was set to 512x512 pixels (except Filament 5, 256x256 pixels) with a scan rate of 0.8 Hz. The data for all filaments were evaluated and depicted with Gwyddion 2.60 SPM software[5], with the images leveled to a plane on a single terrace. Statistical and profile analysis through Gwyddion were performed on the leveled data. Additional experimental details and information regarding the sheet height determination within exfoliated filaments are provided in Supplementary Information Section VI.

Structure Elucidation via Wide-Angle X-ray Scattering: The packing structure of **H-N[5]HDI** was elucidated through X-ray scattering experiments performed at the Beamline 11-3 of the Stanford Synchrotron Radiation Lightsource at the SLAC National Accelerator Laboratory. Full experimental details and analyses are provided in Supplementary Information Section VII.

Fourier-Transform Infrared Spectroscopy (FTIR): FTIR measurements were taken by a Nicolet iS50 spectrometer. Dry ribbons of **H-N[5]HDI** and a dry powder of **EtHex-N[5]HDI** were measured using attenuated total reflection (ATR) and a KBr beam. The spectra and a brief analysis are provided in Supplementary Figure S11. The structure of **EtHex-N[5]HDI** is provided therein.

Cryogenic Transmission Electron Microscopy (Cryo-TEM): See Supplementary Information Section VIII for complete details regarding the measurement and analysis. See subsection Preparation of the Supramolecular Assembly in Supplementary Information Section II for information concerning the preparation of the samples for cryo-TEM.

Density Functional Theory (DFT) Calculations: The DFT geometric optimizations, transition-state searches, intrinsic reaction coordinate (IRC) calculations, and thermochemical calculations were executed by Jaguar, version 13.3.121, release 2022-3, Schrödinger, Inc. on the Sherlock computing cluster at Stanford University[6]. The geometries of the ground states of **H-N[5]HDI** and **EtHex-N[5]HDI** were optimized without symmetry restrictions in the gas phase using the B3LYP-D3 functional and the 6-31G** basis set. Subsequent thermochemical single-point calculations (B3LYP-D3/6-31G**) using the optimized ground-state geometries of **H-N[5]HDI** and **EtHex-N[5]HDI** in the gas phase provided the Gibbs free energies at 298.15 K and 1 atm. The transition-state corresponding to the helical inversion of **H-N[5]HDI** was identified using the quadratic synchronous transit (QST) method at the B3LYP-D3/6-31G** level of theory. The subsequent thermochemical single-point calculation (B3LYP-D3/6-31G**) using the identified transition-state geometry in the gas phase returned a single imaginary frequency. This thermochemical calculation also provided the Gibbs free energy of the transition state of **H-N[5]HDI** at 298.15 K and 1 atm. A subsequent IRC calculation (B3LYP-D3/6-31G**) confirmed that the identified transition state links the left- and right-handed helical geometries of **H-N[5]HDI**. The minima and transition-state geometries of carbo[4]helicene and carbo[5]helicene were previously calculated by Barroso *et al*[7]. These geometries were used in our thermochemical single-point calculations to provide the Gibbs free energies in the gas phase at 298.15 K and 1 atm at the B3LYP-D3/6-31G** level of theory. Our calculations for the minima and transition state geometries reported by Barroso *et al*. returned the anticipated zero (minima) and one (transition states) imaginary frequencies. The Cartesian coordinates and thermochemical properties of the calculated structures are provided in Supplementary Information Section V. For the DFT models of **N[5]HDI**, the 2-ethylhexyl chains were truncated to methyl groups to expedite the calculations.

UV-Visible Absorbance and Fluorescence Spectroscopy: UV-visible spectra were collected by an Agilent Cary 6000i spectrophotometer. Fluorescence spectra were collected by a Horiba Fluorolog-3 spectrofluorometer. Additional experimental conditions are provided in Supplementary Figure S50 in Section IX.

Cyclic Voltammetry (CV): The voltammogram was recorded using a PalmSens4 potentiostat connected to a glassy carbon working electrode, a 0.02-inch diameter platinum counter electrode,

and a 0.02-inch diameter platinum pseudo-reference electrode. Potentials were referenced to an internal ferrocene/ferrocenium redox couple. The voltammogram of **EtHex-N[5]HDI** (see Supplementary Figure S11 for its structure) and additional experimental conditions are provided in Supplementary Figure S51 of Section IX.

Circular Dichroism (CD): The CD spectra were collected by a Jasco J-815 spectropolarimeter. Additional experimental conditions are provided in Supplementary Figure S53 in Section IX.

III. Synthetic Procedures and Characterization Data

*Synthesis of **2***

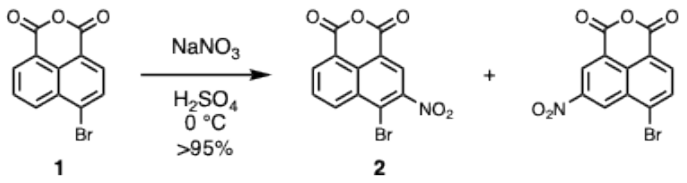

In a 500-mL round-bottom flask equipped with a large stir bar, **1** (50.53 g, 182.4 mmol, 1 equiv.) was dissolved in 250 mL of concentrated sulfuric acid at room temperature. The solution was cooled to 0 ºC, and then sodium nitrate (18.62 g, 219.1 mmol, 1.201 equiv.) was slowly added to the stirring solution over 10 min. The solution was stirred for 3 h under air at 0 °C. The resultant solution was poured over 1 L of packed ice, which precipitated a cream-colored solid. The mixture was stirred for 15 min, and then the solid was collected by vacuum filtration, washed with 5 L of deionized water, and dried *in vacuo* at 90 ºC to yield a cream-colored powder (57.99 g, 180.0 mmol, >95%). ^{1}H NMR revealed a ratio of 84:16 of **2** (48.8 g, 151 mmol, 83.1%) to 4-bromo-6-nitro-1,8-napthalic anhydride, the undesired isomer. HRMS (ESI+) calculated m/z for $[C_{12}H_4NO_5Br+H]^+$ is 321.9346; found 321.9344.

2: ^{1}H NMR (500 MHz, DMSO-d_6, 298 K) δ 8.92 (s, 1H), 8.83 (dd, *J* = 8.6, 1.1 Hz, 1H), 8.74 (dd, *J* = 7.3, 1.1 Hz, 1H), 8.19 (dd, *J* = 8.7, 7.3 Hz, 1H). ^{13}C NMR (101 MHz, DMSO-d_6, 298 K) δ 159.66, 159.06, 149.40, 135.24, 134.92, 130.96, 130.52, 130.48, 125.58, 121.78, 121.11, 120.47.

4-Bromo-6-nitro-1,8-napthalic anhydride: ^{1}H NMR (500 MHz, DMSO-d_6, 298 K) δ 9.28 (d, *J* = 2.2 Hz, 1H), 9.00 (d, *J* = 2.2 Hz, 1H), 8.56 (d, *J* = 7.9 Hz, 1H), 8.46 (d, *J* = 7.9 Hz, 1H). ^{13}C NMR (101 MHz, DMSO-d_6, 298 K) δ 159.38, 159.16, 146.84, 135.39, 133.68, 132.67, 131.58, 129.70, 128.55, 125.01, 122.59, 119.87.

*Synthesis of **3***

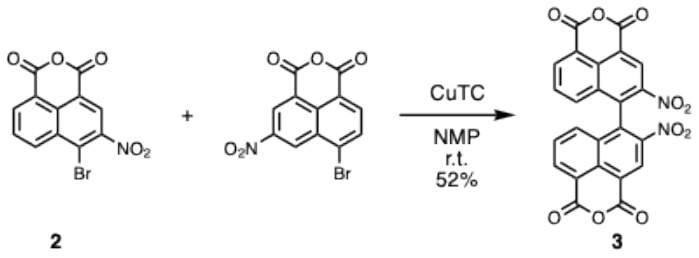

*For the synthesis of **3** to succeed, it is essential that the mixture of **2** and its isomer isolated in the previous step first be crystallized:* Transfer the mixture (~60 g) to a 2-L Erlenmeyer flask equipped with a large stir bar and disperse in acetonitrile (1.6 L). Under a continuous stream of nitrogen, heat the mixture to reflux and then gradually add acetonitrile (200—400 mL) while refluxing until dissolution is achieved. Immerse the Erlenmeyer flask in ice water for 1.5 h to crystallize. Collect the crystals of **2** and 4-bromo-6-nitro-1,8-naphthalic anhydride by vacuum filtration, rinse with 150 mL of ice-cold acetonitrile, and dry overnight *in vacuo*.

In a 1-L Schlenk flask equipped with a large stir bar, the crystalline isomeric mixture of **2** and 4-bromo-6-nitro-1,8-naphthalic anhydride (37.90 g, 85.0% of which was **2**: 32.2 g, 100. mmol, 1 equiv.) was evacuated and backfilled with nitrogen three times. By cannula, 400 mL of nitrogen-sparged, anhydrous NMP were transferred to the flask and stirred. To the resultant stirring solution, copper(I) thiophene-2-carboxylate (57.65 g, 302.3 mmol, 3.02 equiv.) was added through a stream of nitrogen over 2 min. The resultant slurry was concealed from ambient light and then stirred at room temperature under a positive pressure of nitrogen for 4.5 h. *The reaction mixture was protected from ambient light throughout the following work-up:* The reaction mixture was diluted with 500 mL of ethyl acetate and stirred under air for 30 min. The resultant mixture was gravity filtered through a thick, ethyl-acetate-wetted plug of sand and silica. The plug was flushed with ethyl acetate (~700 mL), while applying vacuum, until the eluate was colorless. The ethyl acetate was removed from the product solution under reduced pressure by rotary evaporation at 23 ºC. Then, 1.5 L of ice-chilled, saturated NH_4Cl(aq) were added to the stirring product solution, eliciting the precipitation of a tan solid. This mixture was stirred for 1 h, giving a suspension of fine yellow solid. This solid was collected by vacuum filtration, triturated with 500 mL of saturated NH_4Cl(aq) and then 4 L of water, and dried *in vacuo*. The crude product mixture (29.51 g) was stirred under nitrogen in 400 mL of warm acetone for 30 min. Then, 600 mL of methanol were added to the mixture and stirred at room temperature, under nitrogen, for an additional 15 min. The resultant solid was collected by vacuum filtration and dried *in vacuo*, giving **3** as a fine, cream-colored powder (12.5 g, 25.8 mmol, 51.6%). ^{1}H NMR (400 MHz, DMSO-d_6, 298 K) δ 9.19 (s, 2H), 8.72 (dd, *J* = 7.3, 1.0 Hz, 2H), 7.86 (dd, *J* = 8.6, 7.3 Hz, 2H), 7.60 (dd, *J* = 8.6, 1.1 Hz, 2H). ^{13}C NMR (101 MHz, DMSO-d_6, 298 K) δ 159.63, 159.28, 145.90, 135.26, 133.71, 133.62, 131.36, 130.56, 130.24, 125.83, 122.68, 120.58. HRMS (ESI+) calculated m/z for $[C_{24}H_8N_2O_{10}+H]^+$ is 485.0252; found 485.0245.

*Synthesis of **4***

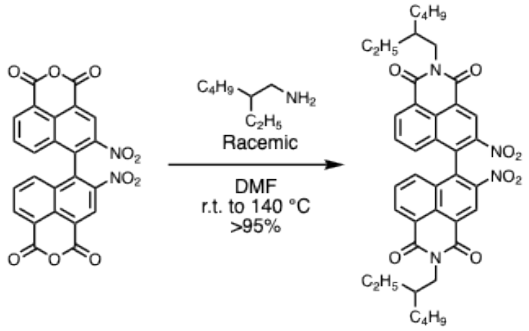

3 **4**

In a 500-mL Schlenk flask equipped with a stir bar, **3** (10.82 g, 22.34 mmol, 1 equiv.) was evacuated and backfilled with nitrogen and then suspended in 170 mL of anhydrous DMF. Then, racemic 2-ethylhexylamine (15.4 mL, 12.2 g, 94.0 mmol, 4.21 equiv.) was added, eliciting the formation of a deep orange solution. This solution was stirred under a positive pressure of nitrogen for 20 min at room temperature, then heated to 140 ºC over 30 min. Upon reaching 140 ºC, the reaction solution was poured over 600 mL of a mixture of ice and HCl(aq), precipitating pale peach-colored solids. The solids were stirred for 15 min under air, collected by vacuum filtration, and triturated with deionized water (10×100 mL) to yield **4** as a pale peach solid (15.21 g, 21.52

mmol, >95%). ^{1}H NMR (400 MHz, $CDCl_3$, 298 K) δ 9.44 (s, 2H), 8.76 (dd, *J* = 7.3, 1.1 Hz, 2H), 7.69 (dd, *J* = 8.6, 7.3 Hz, 2H), 7.37 (dd, *J* = 8.6, 1.1 Hz, 2H), 4.25 – 4.15 (m, 4H), 1.99 (m, 2H), 1.47–1.34 (m, ~16H), 0.98 (t, *J* = 7.4 Hz, 6H), 0.92 (t, *J* = 6.9 Hz, 6H). ^{13}C NMR (101 MHz, $CDCl_3$, 298 K) δ 163.18, 162.39, 145.99, 134.53, 134.29, 132.20, 130.76, 130.02, 129.79, 125.48, 125.44, 123.79, 44.74, 38.07, 30.77, 28.70, 24.05, 23.15, 14.18, 10.64. HRMS (ESI+) calculated m/z for $[C_{40}H_{42}N_4O_8+H]^+$ is 707.3075; found 707.3062.

*Synthesis of **5** and **H-N[5]HDI***

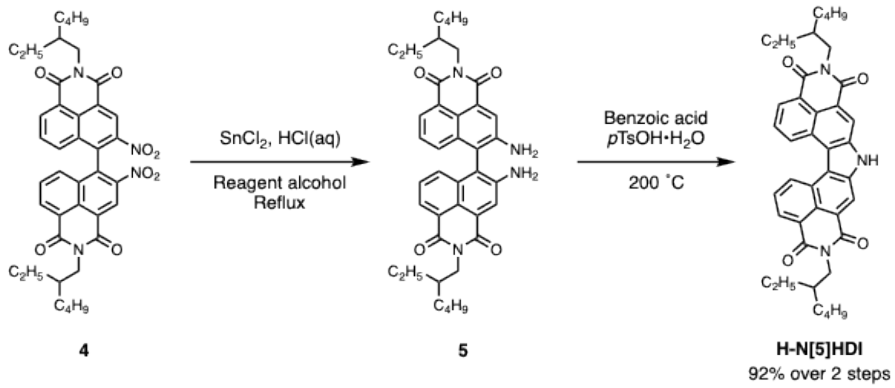

In a 500-mL round-bottom flask equipped with a stir bar, **4** (15.21 g, 21.52 mmol, 1 equiv.) was suspended in 113 mL of reagent alcohol. Then, a solution of tin(II) chloride (42.43 g, 223.8 mmol, 10.40 equiv.) in 86 mL of concentrated HCl(aq) was added to the stirring suspension of **4**. The flask was equipped with a condenser, and the mixture was heated at reflux (oil bath temperature of 95 °C) under air for 3 h. The resultant dark orange solution was poured over 500 mL of deionized water, precipitating a pale yellow solid. The solid was collected by vacuum filtration, triturated with saturated $NaHCO_3$(aq) (2×100 mL) and then water (2×100 mL), and dried *in vacuo* at 110 ºC to yield **5** as a pale yellow-green solid. This crude product was used without additional purification in the subsequent reaction. ^{1}H NMR (400 MHz, DMSO-d_6, 298 K) δ 8.24 (s, 2H), 8.08 (dd, *J* = 1.10, 7.17 Hz, 2H), 7.45 (dd, *J* = 8.5, 7.2 Hz, 2H), 7.20 (dd, *J* = 1.09, 8.50 Hz, 2H), 5.51 (bs, 4H), 4.08–3.89 (m, 4H), 1.92–1.80 (m, ~2H), 1.41–1.20 (m, ~16H), 0.95–0.84 (m, ~12 H). ^{13}C NMR (101 MHz, DMSO-d_6, 298 K) δ 164.12, 163.94, 145.81, 132.29, 129.18, 127.35, 125.28, 122.85, 122.74, 122.24, 121.56, 115.07, 43.08, 37.32, 30.18, 28.11, 23.52, 22.52, 13.98, 10.53. HRMS (ESI+) calculated m/z for $[C_{40}H_{46}N_4O_4+H]^+$ is 647.3592; found 647.3593.

In a 500-mL round-bottom flask equipped with a stir bar, crude **5** (14.94 g of the crude product, <21.52 mmol of **5**, 1 equiv.), benzoic acid (150. g), and *p*-toluenesulfonic acid monohydrate (8.84 g, 46.5 mmol, ~2.2 equiv.) were sealed under air with a greased glass stopper. The top of the flask was insulated with aluminum foil, and then the mixture was heated to 200 °C in a concave anodized aluminum mantle. The resultant molten solution was stirred at 200 °C for 46 h. Then, the temperature was reduced to 60 º C, whereupon the flask was filled to capacity with methanol. This mixture was sonicated for 2 h and then stirred vigorously overnight. The undissolved solids were collected by vacuum filtration and washed with methanol until the filtrate ran colorless, yielding **H-N[5]HDI** as a golden yellow solid (12.45 g, 19.77 mmol, 91.87% from **4**). ^{1}H NMR (400 MHz, $C_2D_2Cl_4$, 373 K) δ 10.01 (bs, 1H), 9.49 (bd, *J* = 8.4 Hz, 2H), 9.00 (bs, 2H), 8.72 (bd, *J* = 7.3 Hz, 2H), 8.02 (bt, *J* = 7.9 Hz, 2H), 4.33–4.20 (bm, 4H), 2.17–2.05 (bm, 2H), 1.59–1.31 (bm, ~16H),

1.03 (bt, *J* = 7.3 Hz, 6H), 0.94 (bt, *J* = 6.9 Hz, 6H). ^{13}C NMR (101 MHz, CD_2Cl_4, 373 K) δ 164.44, 164.13, 137.65, 129.62, 128.41, 127.36, 126.74, 124.99, 123.85, 122.25, 121.10, 118.08, 44.59, 38.04, 30.96, 28.63, 24.29, 22.81, 13.68, 10.60. HRMS (ESI-) calculated m/z for $[C_{40}H_{43}N_3O_4\text{-}H]^-$ is 628.3181; found 628.3170.

Synthesis of ***EtHex-N[5]HDI***

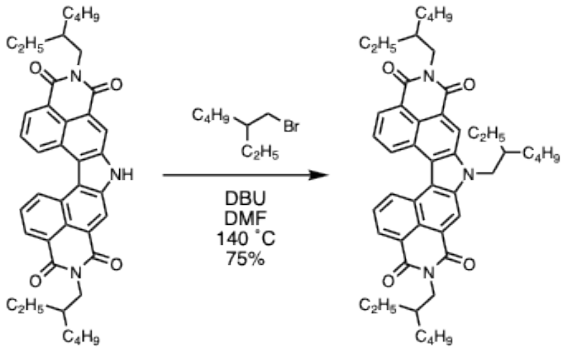

H-N[5]HDI **EtHex-N[5]HDI**

In a 25-mL Schlenk tube equipped with a stir bar and rubber septum, **H-N[5]HDI** (100. mg, 0.159 mmol, 1 equiv.) was suspended in 0.9 mL of anhydrous DMF under a positive pressure of nitrogen. While stirring, 1,8-diazabicyclo[5.4.0]undec-7-ene (0.05 mL, 50 mg, 0.3 mmol, 2 equiv.) was added, resulting in the formation of a red solution. This solution was heated to 60 ºC, whereupon 1-bromo-2-ethylhexane (0.11 mL, 120 mg, 0.62 mmol, 3.9 equiv.) was added dropwise. The mixture was heated at 140 º C for 19.5 h while stirring under a positive pressure of nitrogen. The resultant mixture was diluted with deionized water and DCM, washed with 2 M HCl(aq) and then brine in a separatory funnel, dried over sodium sulfate, and filtered. The solvents were removed under reduced pressure. Purification by column chromatography on silica gel (gradient of 100% hexanes to 100% DCM) yielded **EtHex-N[5]HDI** as a yellow solid (88.0 mg, 0.119 mmol, 74.6%). ^{1}H NMR (400 MHz, $CDCl_3$, 298 K) δ 9.44 (d, *J* = 8.4 Hz, 2H), 8.91 (s, 2H), 8.66 (d, *J* = 7.3 Hz, 2H), 7.95 (t, *J* = 7.9 Hz, 2H), 4.71–4.58 (m, 2H), 4.24–4.13 (m, 4H), 2.27–2.14 (m, 1H), 2.07–1.96 (m, 2H), 1.53–1.17 (m, ~24H), 1.00–0.86 (m, 15H), 0.83 (t, *J* = 7.2 Hz, 3H). ^{13}C NMR (101 MHz, $CDCl_3$, 298 K) δ 164.90, 164.61, 138.99, 129.79, 128.59, 127.53, 126.93, 124.81, 123.67, 121.74, 120.67, 116.95, 44.52, 40.48, 38.10, 30.88, 30.81, 28.82, 28.46, 24.29, 24.21, 23.16, 23.05, 14.17, 13.96, 10.90, 10.78, 10.76. HRMS (ESI+) calculated m/z for $[C_{48}H_{59}N_3O_4\text{+}H]^+$ is 742.4578; found 742.4565.

Synthesis of ***EtHex-NI***

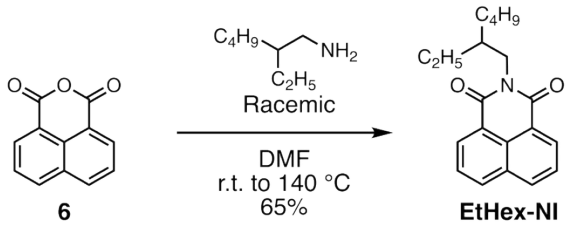

In a 25-mL Schlenk flask equipped with a stir bar, **6** (100. mg, 0.505 mmol, 1 equiv.) was evacuated and backfilled with nitrogen and then suspended in 3.9 mL of anhydrous DMF. Then, racemic 2-ethylhexylamine (0.30 mL, 0.24 g, 1.9 mmol, 3.8 equiv.) was added, eliciting the formation of a deep orange solution. This solution was stirred under a positive pressure of nitrogen for 20 min at room temperature, then heated to 140 ºC over 30 min. Upon reaching 140 ºC, the reaction solution was poured over 60 mL of a mixture of ice and HCl(aq), precipitating solids. The solids were stirred for 15 min under air, collected by vacuum filtration, and triturated with deionized water (3×30 mL) to yield **EtHex-NI** as an off-white solid (102 mg, 0.330 mmol, 65.3%). ^{1}H NMR (500 MHz, $CDCl_3$, 298 K) δ 8.61 (dd, *J* = 7.3, 1.1 Hz, 2H), 8.21 (dd, *J* = 8.4, 1.1 Hz, 2H), 7.76 (dd, *J* = 8.2, 7.2 Hz, 2H), 4.13 (m, 2H), 1.95 (m, 1H), 1.44–1.27 (m, 8H), 0.93 (t, *J* = 7.4 Hz, 3H), 0.88 (t, *J* = 7.1 Hz, 3H). This spectrum matches the ^{1}H NMR previously reported for **EtHex-NI**.[8]

IV. ^{1}H-NMR and ^{13}C-NMR Spectra

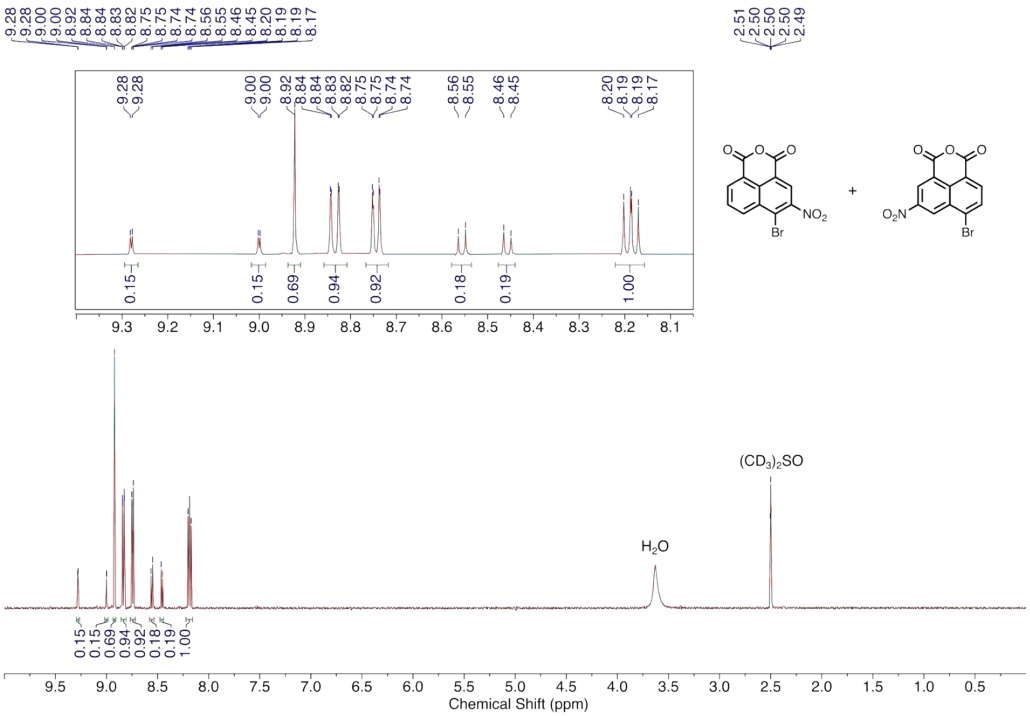

Supplementary Figure S15. ^{1}H-NMR ($(CD_3)_2SO$, 298 K) spectrum of **2** and its undesired isomer.

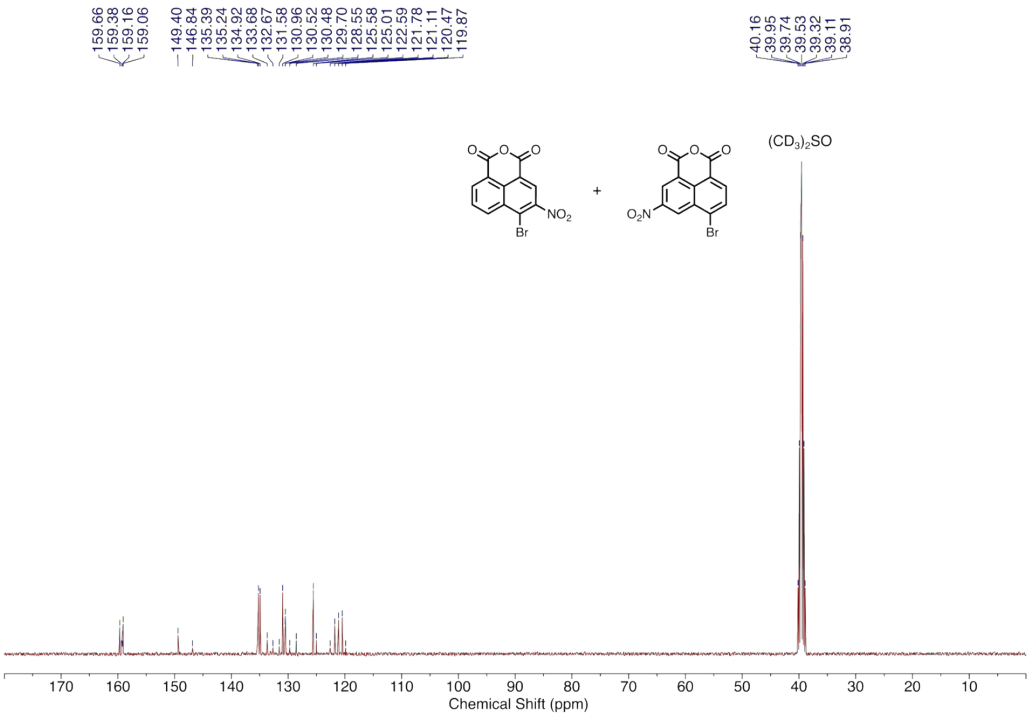

Supplementary Figure S16. ^{13}C-NMR ($(CD_3)_2SO$, 298 K) spectrum of **2** and its undesired isomer.

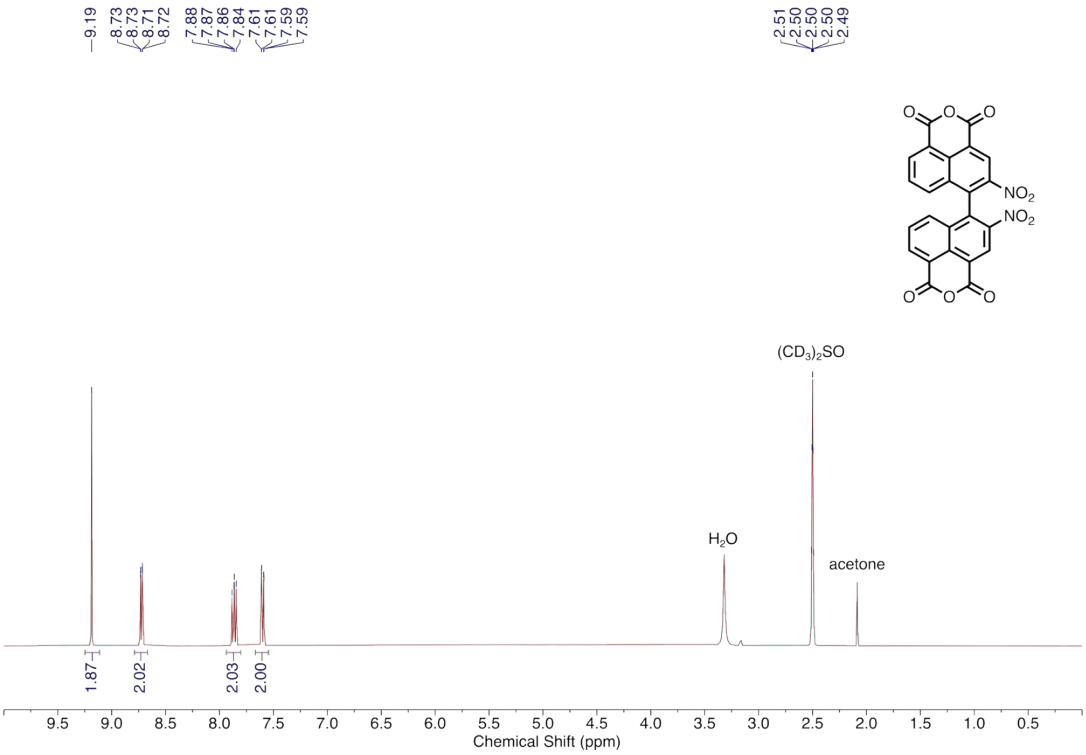

Supplementary Figure S17. ^{1}H-NMR ($(CD_3)_2SO$, 298 K) spectrum of **3**.

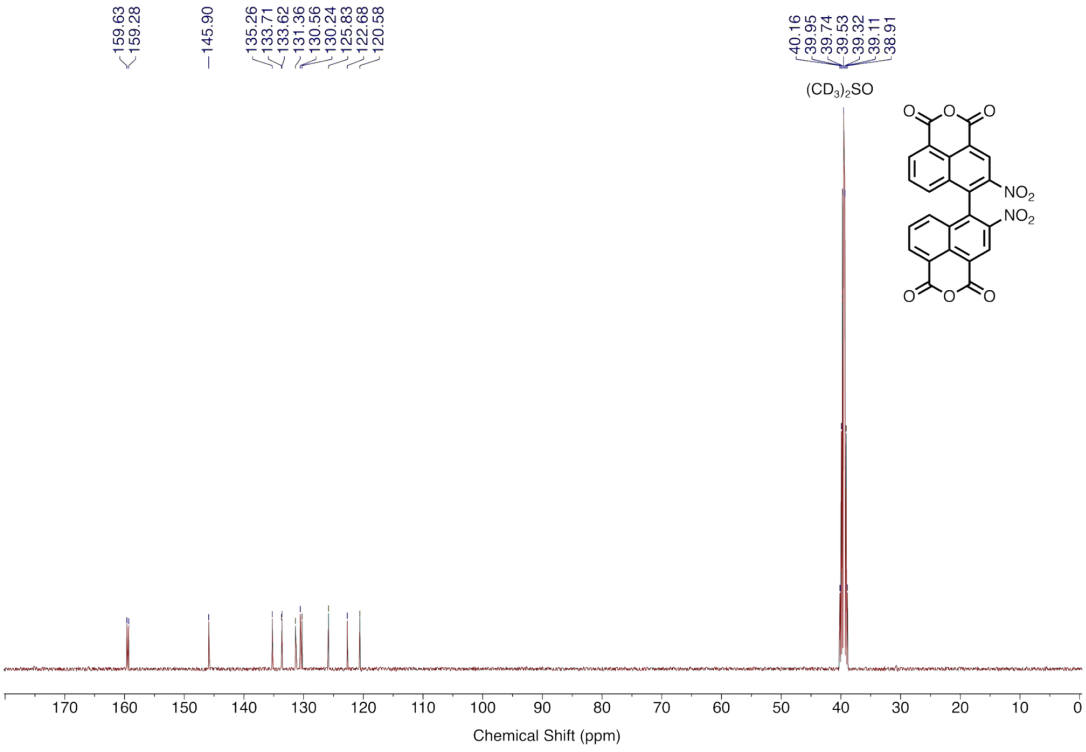

Supplementary Figure S18. ^{13}C-NMR ($(CD_3)_2SO$, 298 K) spectrum of **3**.

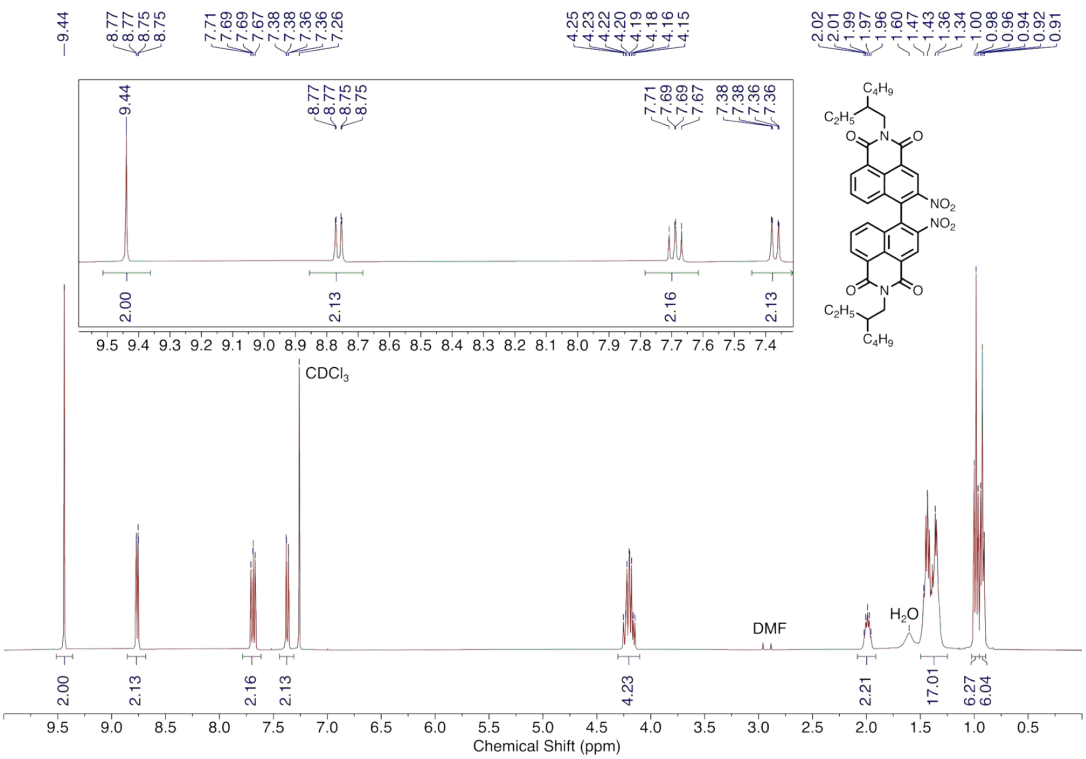

Supplementary Figure S19. ^{1}H-NMR ($CDCl_3$, 298 K) spectrum of **4**.

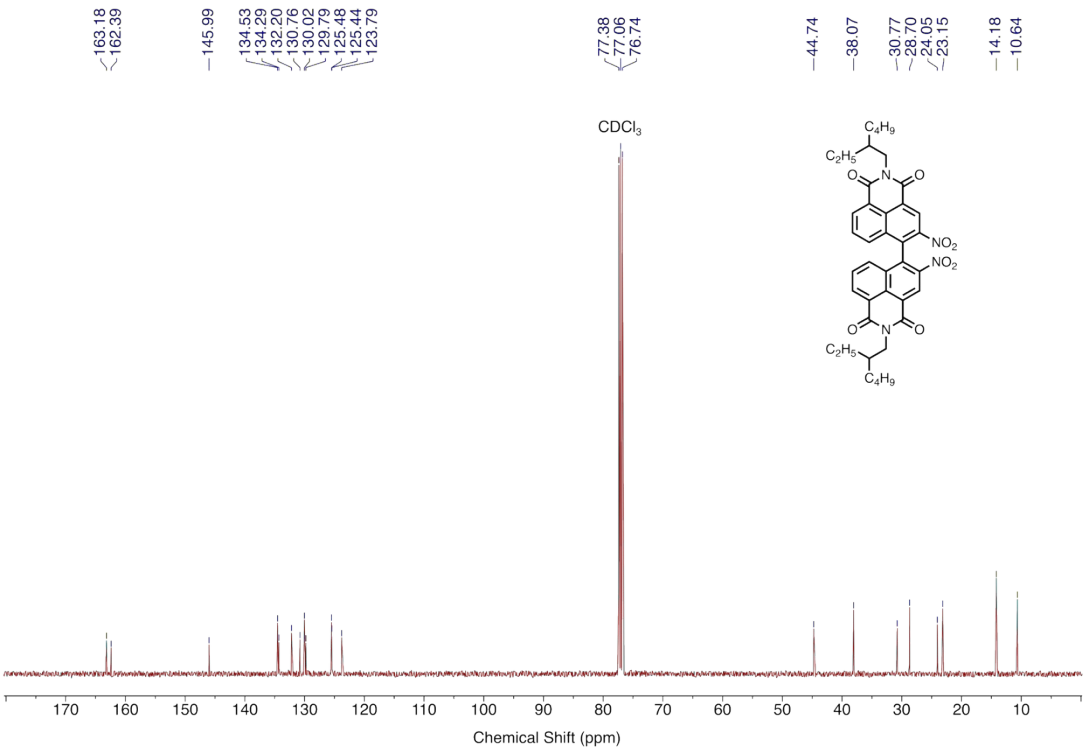

Supplementary Figure S20. ^{13}C-NMR ($CDCl_3$, 298 K) spectrum of **4**.

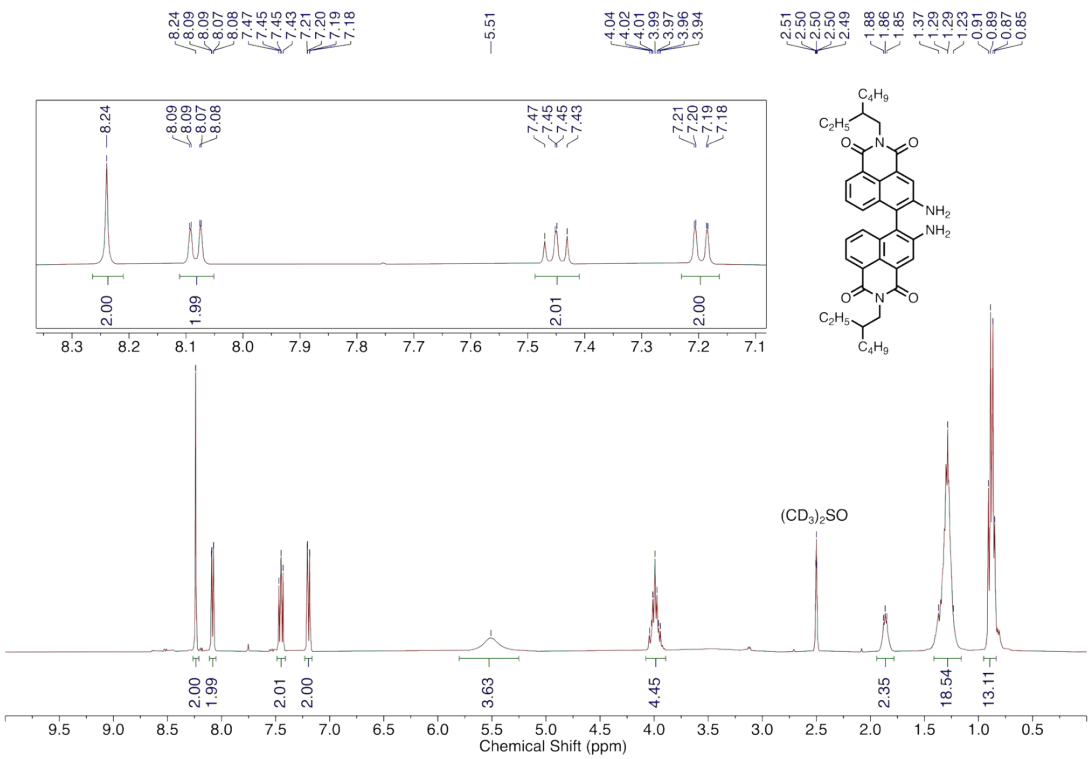

Supplementary Figure S21. ^{1}H-NMR ($(CD_3)_2SO$, 298 K) spectrum of **5**.

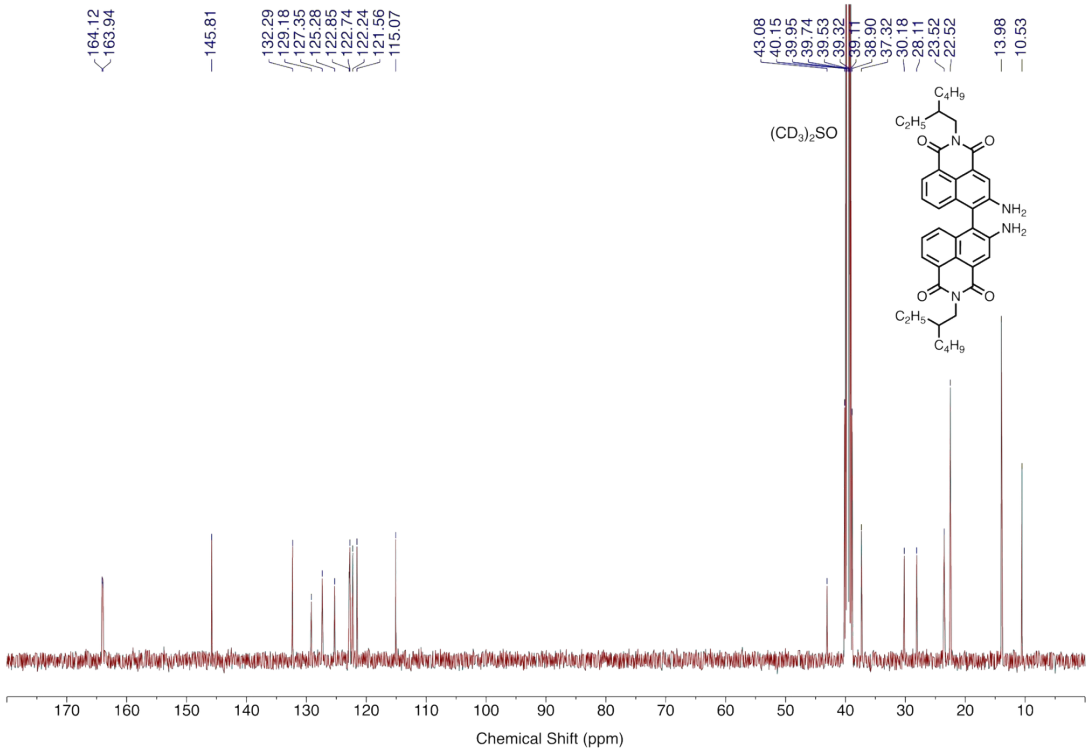

Supplementary Figure S22. ^{13}C-NMR ($(CD_3)_2SO$, 298 K) spectrum of **5**.

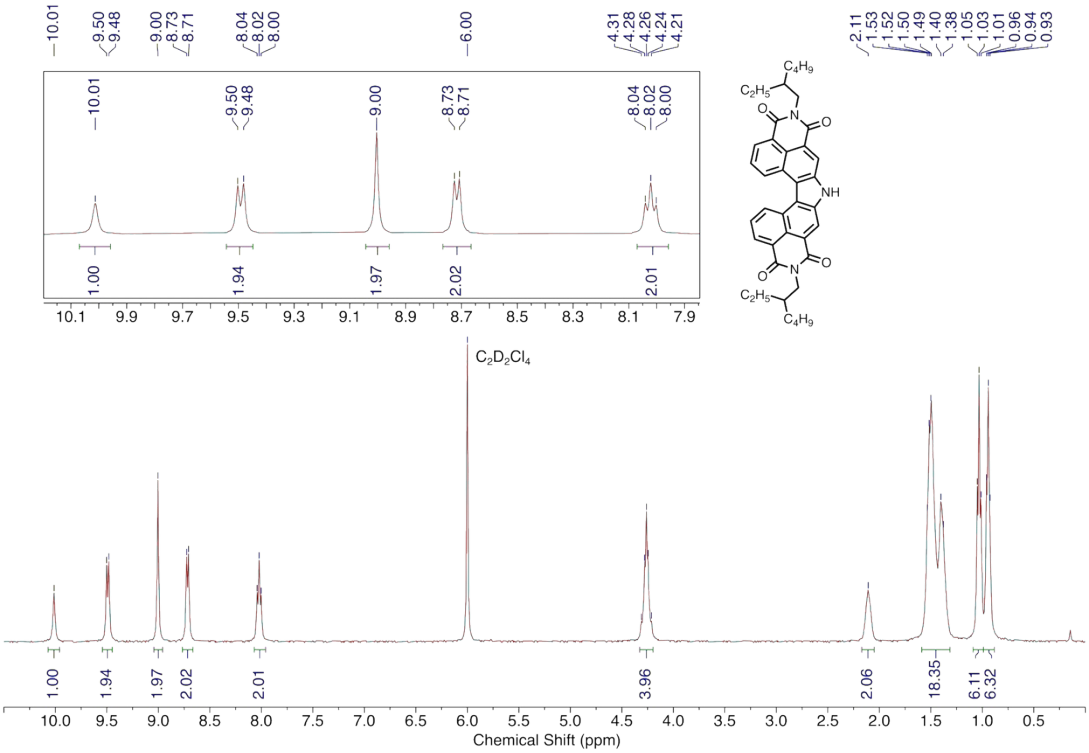

Supplementary Figure S23. ^{1}H-NMR ($C_2D_2Cl_4$, 373 K) spectrum of **H-N[5]HDI**.

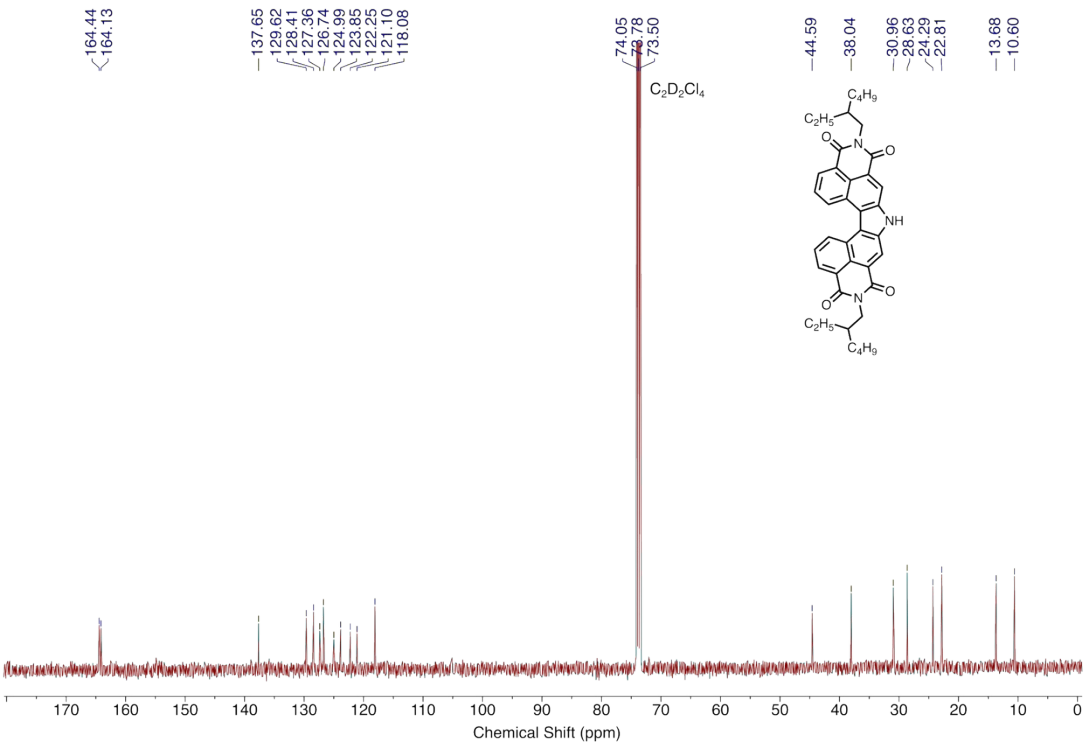

Supplementary Figure S24. ^{13}C-NMR ($C_2D_2Cl_4$, 373 K) spectrum of **H-N[5]HDI**.

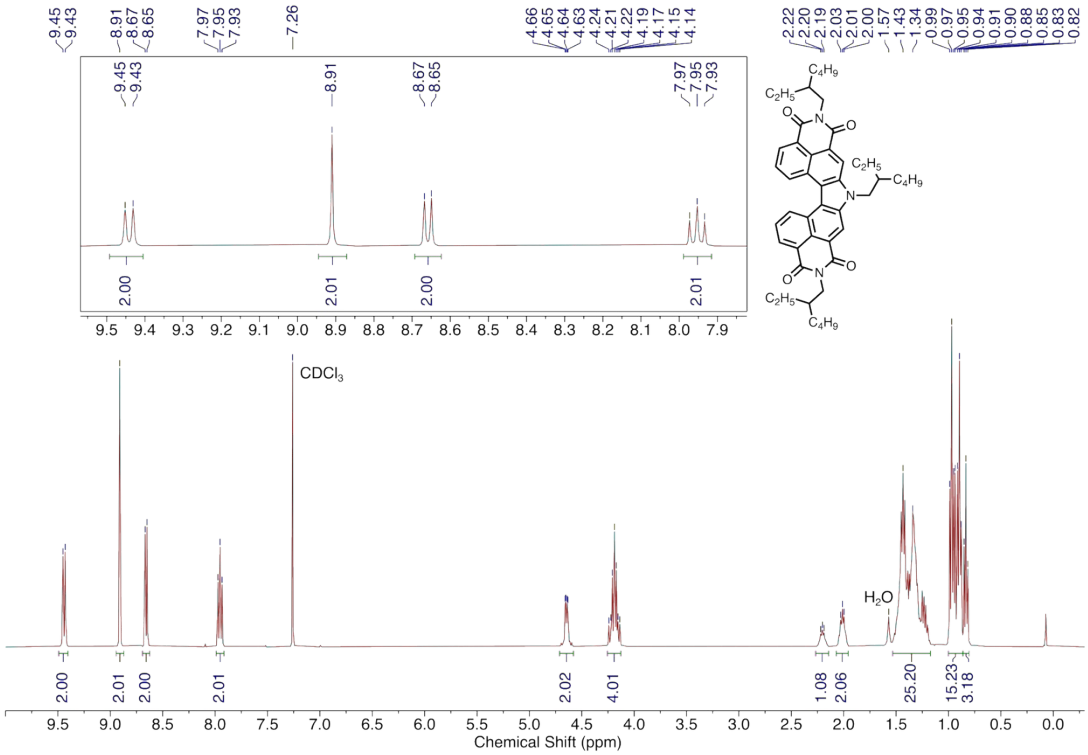

Supplementary Figure S25. ^{1}H-NMR ($CDCl_3$, 298 K) spectrum of **EtHex-N[5]HDI**.

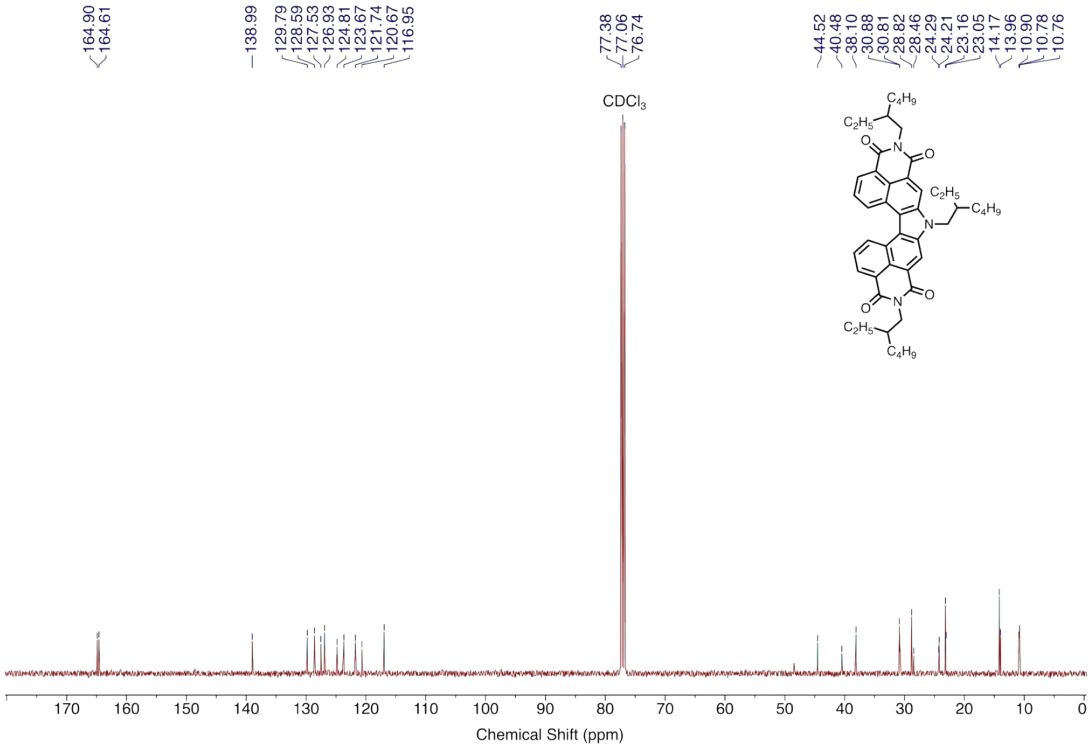

Supplementary Figure S26. ^{13}C-NMR ($CDCl_3$, 298 K) spectrum of **EtHex-N[5]HDI**.

V. DFT Calculations: Structures and Thermochemistry

a. H-N[5]HDI Minimum

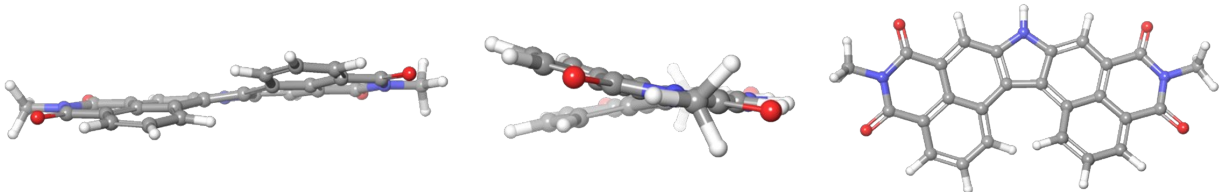

Supplementary Figure S27. DFT-optimized (B3LYP-D3/6-31G**) structure of left-handed **H-N[5]HDI** from different perspectives ($\Delta G_{298.15\,K}$ = -1464.857050 hartrees).

Supplementary Table S1.

Coordinates of Left-Handed **H-N[5]HDI** (from left-to-right: atom, x, y, z in Å)

C1	-4.0367	-2.5909	-0.0137	C25	-11.4040	1.4489	-1.0633
C2	-4.8431	-1.4688	-0.0762	N26	-11.3916	2.7730	-0.6053
C3	-4.2955	-0.1670	-0.1699	C27	-10.2390	3.4965	-0.2773
C4	-2.8702	-0.0453	-0.0785	O28	-0.2050	2.4386	0.2379
C5	-2.0632	-1.2094	-0.0427	O29	0.1373	-2.1060	-0.0102
C6	-2.6397	-2.4688	-0.0296	O30	-12.4669	0.9119	-1.3443
C7	-5.0695	1.0447	-0.2421	O31	-10.2990	4.6680	0.0752
C8	-4.3955	2.2671	0.0088	C32	-12.6976	3.4321	-0.5008
C9	-3.0033	2.3821	0.1295	C33	1.4269	0.3258	0.1532
C10	-2.2481	1.2341	0.0417	H34	-4.4909	-3.5737	0.0636
N11	-5.3208	3.2818	0.0849	H35	-5.9154	-1.5867	-0.0053
C12	-6.5757	2.7695	-0.1454	H36	-1.9913	-3.3369	0.0026
C13	-6.4647	1.3833	-0.4246	H37	-2.5099	3.3372	0.2748
C14	-7.6494	0.7015	-0.8769	H38	-7.8515	4.5138	0.1653
C15	-8.8969	1.4023	-0.7914	H39	-6.7226	-1.0670	-1.6997
C16	-8.9484	2.7669	-0.3735	H40	-8.8104	-2.1445	-2.3774
C17	-7.7930	3.4626	-0.0955	H41	-11.0074	-0.9802	-2.0111
C18	-7.6611	-0.5710	-1.4960	H42	-12.5372	4.4384	-0.1223
C19	-8.8407	-1.1699	-1.9003	H43	-13.3408	2.8624	0.1726
C20	-10.0704	-0.5211	-1.7167	H44	-13.1746	3.4628	-1.4827
C21	-10.0950	0.7577	-1.1857	H45	1.8707	-0.6642	0.0874
C22	-0.7728	1.3583	0.1319	H46	1.7042	0.8101	1.0920
N23	-0.0307	0.1753	0.0861	H47	1.7671	0.9581	-0.6693
C24	-0.5797	-1.1151	0.0097	H48	-5.1076	4.2461	0.2845

b. H-N[5]HDI Inversion Transition State

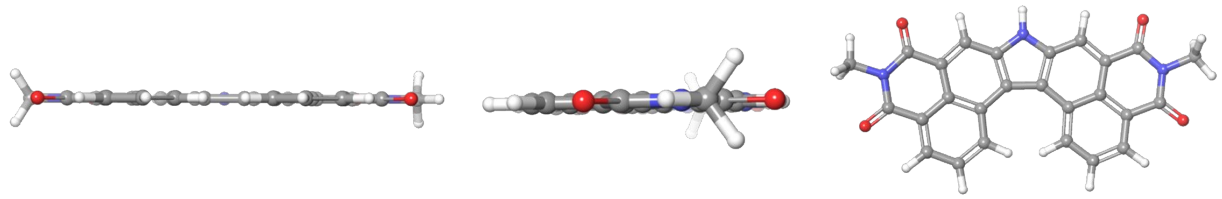

Supplementary Figure S28. Transition-state (B3LYP-D3/6-31G**) structure for the helical inversion of **H-N[5]HDI** from different perspectives ($\Delta G_{298.15\,K}$ = -1464.851121 hartrees).

Supplementary Table S2.

Coordinates of Transition-State **H-N[5]HDI** (from left-to-right: atom, x, y, z in Å)

C1	1.5982	-2.8188	-2.5388	C25	-3.2477	4.4799	-1.432
C2	0.9722	-1.7913	-1.8574	N26	-3.3655	4.8608	-0.0902
C3	1.0222	-1.649	-0.4518	C27	-2.7887	4.1763	0.9782
C4	1.7793	-2.657	0.2482	O28	2.8043	-3.6484	3.6158
C5	2.4147	-3.7042	-0.4672	O29	3.7559	-5.6684	-0.3587
C6	2.3277	-3.7882	-1.846	O30	-2.9425	4.578	2.1251
C7	0.3871	-0.594	0.3251	O31	-3.7829	5.1286	-2.3211
C8	0.5858	-0.6694	1.7304	H32	1.5182	-2.8668	-3.6202
C9	1.3219	-1.6498	2.4048	H33	0.4282	-1.0794	-2.4453
C10	1.9158	-2.6393	1.6662	H34	2.8284	-4.6047	-2.3533
N11	-0.0534	0.3672	2.3486	H35	1.4301	-1.6425	3.4840
C12	-0.6756	1.1367	1.4072	H36	-1.5578	2.6349	2.7172
C13	-0.4457	0.5988	0.1117	H37	-0.4195	0.1343	-2.6632
C14	-1.0587	1.3316	-0.9863	H38	-1.4781	1.4255	-4.3889
C15	-1.8296	2.5119	-0.6794	H39	-2.8124	3.476	-3.8035
C16	-1.9981	2.9657	0.6602	C40	4.0697	-5.7165	2.2936
C17	-1.4242	2.2822	1.7000	C41	-4.1436	6.0568	0.2473
C18	-0.9752	0.9982	-2.3577	H42	4.0557	-5.5163	3.3616
C19	-1.583	1.7384	-3.355	H43	3.6322	-6.6932	2.0783
C20	-2.3264	2.8791	-3.0407	H44	5.0925	-5.7099	1.9123
C21	-2.4469	3.2599	-1.7157	H45	-4.5275	6.4799	-0.6771
C22	2.6918	-3.6703	2.3965	H46	-4.9623	5.7847	0.9167
N23	3.2893	-4.6692	1.6253	H47	-3.505	6.7754	0.7651
C24	3.1989	-4.7534	0.2331	H48	-0.0659	0.5362	3.3418

c. Carbo[4]helicene Minimum

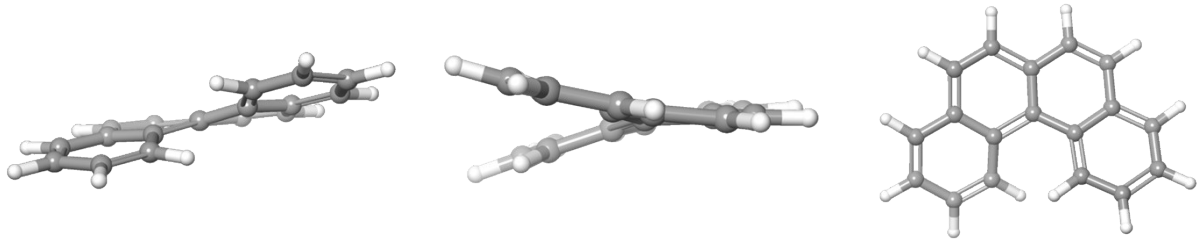

Supplementary Figure S29. DFT-optimized structure of left-handed carbo[4]helicene, from different perspectives, reported by Barroso *et al*[7]. In the gas phase at the B3LYP-D3/6-31G** level of theory, $\Delta G_{298.15\,K}$ = -693.010144 hartrees.

Supplementary Table S3.

Coordinates of Left-Handed Carbo[4]helicene (from left-to-right: atom, x, y, z in Å)

C1	-2.3944	-0.1138	2.903	C25	2.4391	-0.0045	1.5121
C2	-1.2221	-0.0704	3.5886	C26	1.2594	0.1437	0.8149
C3	-2.4349	0.1186	1.4965	H27	3.3717	-0.1603	3.4613
C4	0.0125	0.0709	2.8922	H28	1.2086	-0.1540	4.6684
C5	-1.2526	0.4303	0.7893	H29	3.3744	-0.0995	0.9669
C6	0.0112	0.2530	1.4762	H30	1.2879	0.1143	-0.2675
C7	-3.6833	0.0326	0.8124				
C8	-3.7716	0.2755	-0.5215				
C9	-2.6402	0.7581	-1.2401				
C10	-1.3865	0.9057	-0.5732				
H11	-3.3324	-0.3006	3.4205				
H12	-1.2014	-0.2052	4.6674				
H13	-4.5625	-0.2599	1.3817				
H14	-4.7172	0.1668	-1.0471				
C15	-2.7738	1.1620	-2.5866				
C16	-0.3716	1.6113	-1.2654				
C17	-0.5373	2.0271	-2.5691				
C18	-1.7355	1.7678	-3.2551				
H19	-3.7322	1.0113	-3.0785				
H20	0.5365	1.8871	-0.7433				
H21	0.2600	2.5785	-3.0601				
H22	-1.8545	2.0825	-4.2881				
C23	2.4374	-0.0608	2.9158				
C24	1.2367	-0.0451	3.5865				

d. Carbo[4]helicene Inversion Transition State

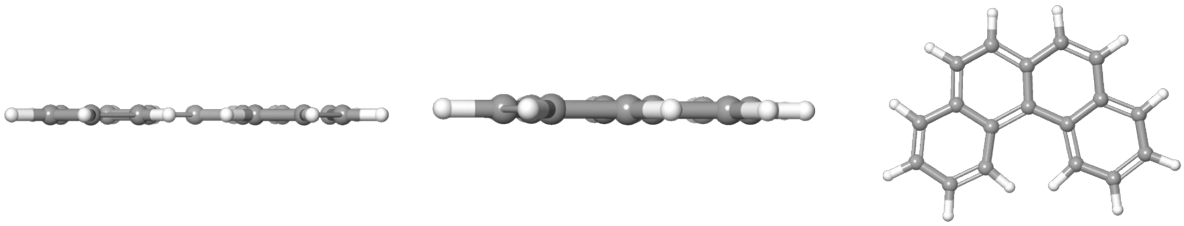

Supplementary Figure S30. Transition-state structure for the helical inversion of carbo[4]helicene, from different perspectives, reported by Barroso *et al*[7]. In the gas phase at the B3LYP-D3/6-31G** level of theory, $\Delta G_{298.15\,K}$ = -693.002892 hartrees.

Supplementary Table S4.

Coordinates of Transition-State Carbo[4]helicene (from left-to-right: atom, x, y, z in Å)

C1	-2.4996	-0.0112	1.2045	C25	1.7296	0.0084	1.569
C2	-1.8975	-0.008	2.4151	H26	1.8882	0.0103	4.9703
C3	-1.7389	-0.0081	-0.0001	H27	-0.5741	-0.0012	4.6462
C4	-0.48	-0.0015	2.5008	H28	3.3552	0.0164	2.9416
C5	-0.3177	-0.0016	0	H29	2.4423	0.0109	-0.7666
C6	0.3326	0.0019	1.3169	H30	2.4422	0.0114	0.7669
C7	-2.4995	-0.0121	-1.2048				
C8	-1.8972	-0.0097	-2.4153				
C9	-0.4797	-0.0032	-2.5009				
C10	0.3327	0.0009	-1.3169				
H11	-3.5836	-0.0163	1.123				
H12	-2.4789	-0.0104	3.3337				
H13	-3.5835	-0.017	-1.1234				
H14	-2.4785	-0.0127	-3.334				
C15	0.0976	-0.001	-3.7905				
C16	1.7298	0.0073	-1.5688				
C17	2.2739	0.0094	-2.8356				
C18	1.4574	0.0052	-3.9732				
H19	-0.5736	-0.0044	-4.6463				
H20	3.3555	0.0143	-2.9412				
H21	1.8888	0.0068	-4.9701				
C22	1.457	0.008	3.9734				
C23	0.0972	0.0016	3.7905				
C24	2.2736	0.0114	2.8359				

e. Carbo[5]helicene Minimum

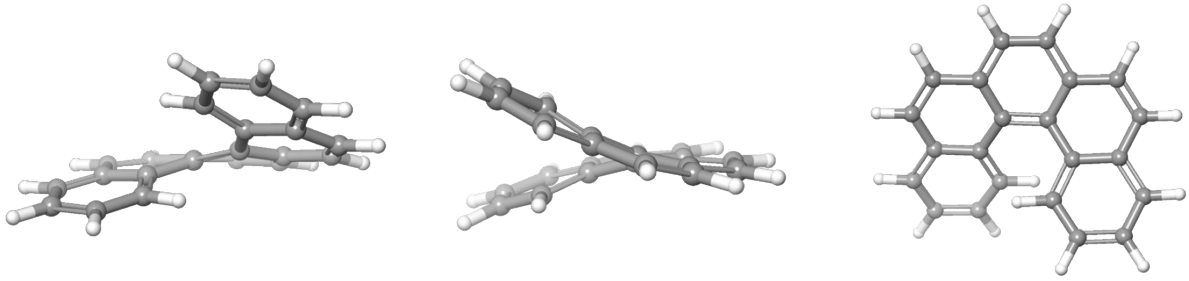

Supplementary Figure S31. DFT-optimized structure of left-handed carbo[5]helicene, from different perspectives, reported by Barroso *et al*[7]. In the gas phase at the B3LYP-D3/6-31G** level of theory, $\Delta G_{298.15\,K}$ = -846.612500 hartrees.

Supplementary Table S5.

Coordinates of Left-Handed Carbo[5]helicene (from left-to-right: atom, x, y, z in Å)

C1	-2.3692	-0.2066	2.8543	C25	2.5116	-0.0023	1.5073
C2	-1.1986	-0.0475	3.5328	C26	1.3069	-0.1023	0.7535
C3	-2.4143	-0.0184	1.4474	C27	3.7571	-0.2037	0.871
C4	0.0247	0.1039	2.8276	C28	3.827	-0.5764	-0.4509
C5	-1.2321	0.2965	0.7323	C29	2.6376	-0.789	-1.1703
C6	0.0317	0.1318	1.4108	C30	1.4139	-0.5598	-0.5815
C7	-3.6646	-0.1111	0.7648	H31	3.3773	0.301	3.4743
C8	-3.7698	0.1849	-0.5567	H32	1.1988	0.2449	4.6396
C9	-2.6561	0.735	-1.2569	H33	4.6638	-0.0918	1.4614
C10	-1.3966	0.8508	-0.6013	H34	4.7903	-0.7413	-0.9256
H11	-3.2962	-0.416	3.3823	H35	0.5109	-0.7515	-1.1488
H12	-1.1718	-0.0976	4.6186	H36	2.6796	-1.1479	-2.195
H13	-4.535	-0.4321	1.3322				
H14	-4.7195	0.0866	-1.0769				
C15	-2.8179	1.2489	-2.5632				
C16	-0.4012	1.6261	-1.2425				
C17	-0.5947	2.1522	-2.5004				
C18	-1.8022	1.9344	-3.1873				
H19	-3.7801	1.1209	-3.054				
H20	0.5292	1.8256	-0.7241				
H21	0.1898	2.7493	-2.9572				
H22	-1.9431	2.3364	-4.1869				
C23	2.4488	0.2087	2.9161				
C24	1.2502	0.1895	3.5548				

f. Carbo[5]helicene Inversion Transition State

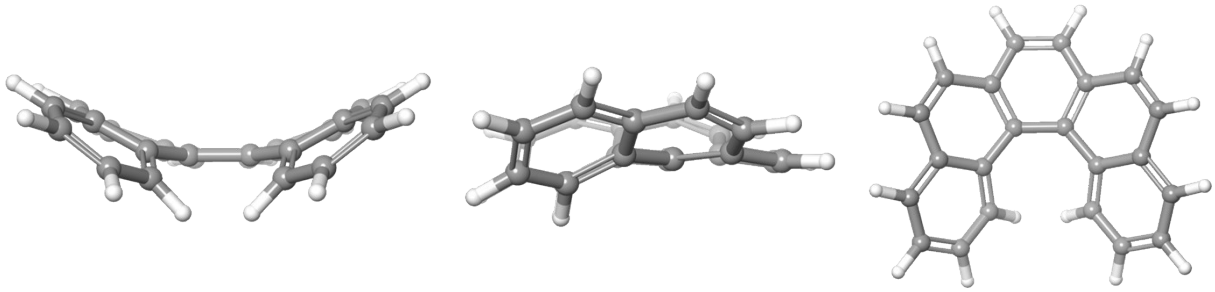

Supplementary Figure S32. Transition-state structure for the helical inversion of carbo[5]helicene, from different perspectives, reported by Barroso *et al*[7]. In the gas phase at the B3LYP-D3/6-31G** level of theory, $\Delta G_{298.15\,K}$ = -846.573443 hartrees.

Supplementary Table S6.

Coordinates of Transition-State Carbo[5]helicene (from left-to-right: atom, x, y, z in Å)

C1	3.1712	-0.7004	-0.6145	C25	-0.2711	0.4801	2.8891
C2	3.1512	-0.6668	0.7417	C26	-0.4692	-0.2293	1.6598
C3	1.9843	-0.445	-1.3388	C27	-1.3692	0.8621	3.6874
C4	1.9436	-0.3767	1.4172	C28	-2.6501	0.4545	3.3918
C5	0.7003	-0.4639	-0.7126	C29	-2.8285	-0.4278	2.3216
C6	0.6787	-0.4276	0.7551	C30	-1.7664	-0.7596	1.5022
C7	2.1707	-0.0099	-2.6881	H31	1.1678	1.1692	4.3628
C8	1.1433	0.5022	-3.4016	H32	3.0929	0.16	3.1673
C9	-0.1854	0.3363	-2.9159	H33	-1.1698	1.4467	4.5826
C10	-0.4202	-0.3115	-1.6594	H34	-3.4868	0.7465	4.0199
H11	4.1054	-0.8054	-1.1601	H35	-1.9303	-1.5394	0.7842
H12	4.0688	-0.744	1.3192	H36	-3.7986	-0.8826	2.1411
H13	3.185	0.0053	-3.0787				
H14	1.2968	0.9527	-4.3789				
C15	-1.2593	0.6776	-3.7641				
C16	-1.7219	-0.8342	-1.5141				
C17	-2.7591	-0.5441	-2.3798				
C18	-2.5487	0.2842	-3.4866				
H19	-1.0332	1.2172	-4.681				
H20	-1.9075	-1.5777	-0.7635				
H21	-3.7345	-0.9901	-2.2057				
H22	-3.3663	0.5442	-4.1528				
C23	1.0429	0.6709	3.4049				
C24	2.0905	0.1249	2.7483				

g. EtHex-N[5]HDI Minimum

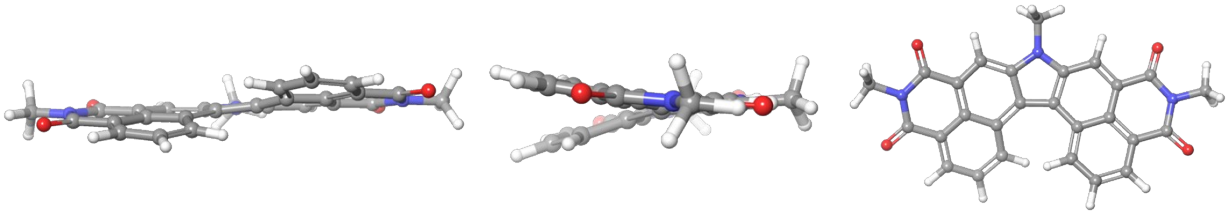

Supplementary Figure S33. DFT-optimized (B3LYP-D3/6-31G**) structure of left-handed **EtHex-N[5]HDI** from different perspectives ($\Delta G_{298.15\,K}$ = -1504.147485 hartrees).

Supplementary Table S7.

Coordinates of Left-Handed **EtHex-N[5]HDI** (from left-to-right: atom, x, y, z in Å)

C1	-4.0471	-2.5874	-0.0008	C27	-10.2412	3.4928	-0.2875
C2	-4.8517	-1.4631	-0.0484	O28	-0.2045	2.4352	0.2182
C3	-4.3031	-0.1616	-0.1463	O29	0.128	-2.1092	-0.0447
C4	-2.8767	-0.0437	-0.0698	O30	-12.4552	0.9026	-1.3718
C5	-2.0718	-1.2101	-0.0492	O31	-10.3072	4.6657	0.0602
C6	-2.6502	-2.4691	-0.0358	C32	-12.6971	3.4248	-0.5403
C7	-5.0741	1.0517	-0.2113	C33	1.4215	0.3205	0.11
C8	-4.4009	2.2751	0.043	H34	-4.5028	-3.5693	0.0798
C9	-3.0053	2.3842	0.1465	H35	-5.9234	-1.5789	0.0362
C10	-2.2527	1.2345	0.0463	H36	-2.003	-3.3384	-0.0156
N11	-5.3183	3.2987	0.1378	H37	-2.5025	3.3348	0.2829
C12	-6.5731	2.7795	-0.11	H38	-7.8784	4.5134	0.1797
C13	-6.4645	1.3918	-0.3945	H39	-6.7015	-1.0579	-1.6752
C14	-7.6424	0.7058	-0.8573	H40	-8.7783	-2.1434	-2.3716
C15	-8.8927	1.4003	-0.7832	H41	-10.9834	-0.9885	-2.0245
C16	-8.9491	2.764	-0.3659	H42	-12.5423	4.4331	-0.165
C17	-7.7984	3.4631	-0.0747	H43	-13.3472	2.8574	0.1285
C18	-7.6435	-0.5659	-1.479	H44	-13.163	3.4498	-1.5276
C19	-8.8169	-1.1693	-1.8941	H45	1.8635	-0.6699	0.0384
C20	-10.0509	-0.5259	-1.7212	H46	1.7103	0.804	1.0458
C21	-10.0847	0.7528	-1.1903	H47	1.7534	0.953	-0.7159
C22	-0.7764	1.3565	0.1172	C48	-4.9844	4.6901	0.3839
N23	-0.0368	0.1721	0.0596	H49	-5.8794	5.2355	0.6812
C24	-0.5881	-1.1177	-0.0138	H50	-4.5641	5.1607	-0.5113
C25	-11.3957	1.4413	-1.0817	H51	-4.2574	4.7592	1.197
N26	-11.3892	2.7669	-0.6269				

VI. Atomic Force Microscopy and Sheet Height Determination

To determine the average sheet height, we first processed the data from a single exfoliated filament of **H-N[5]HDI** with well-defined terraces ("Filament 1") in three different ways (Supplementary Figure S34). First, the raw, unleveled image was zeroed at the substrate height and used without further adjustment. Second, the image was plane fit to terrace five, as it is the largest and most distinguishable terrace, then zeroed to the lowest discernable terrace height. Third, a small portion of the same filament was re-measured at higher resolution and plane fit to terrace five. We performed height analysis across all three images to ensure that (1) leveling the terraces still provided a fair representation by comparing to the unleveled terraces, and (2) individual terraces could be well identified across the image processing methods.

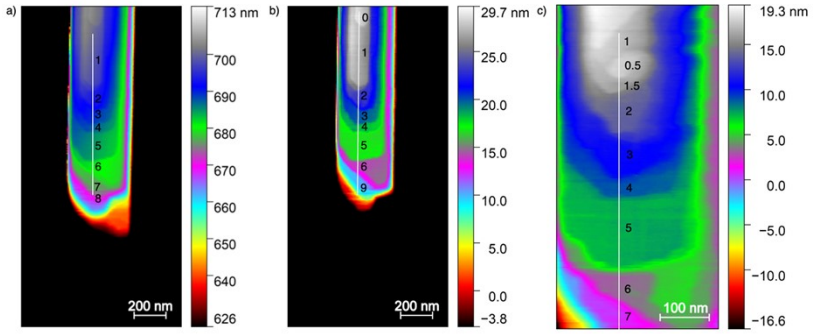

Supplementary Figure S34. AFM images of **H-N[5]HDI** filament terraces after exfoliation, processed by (**a**) zeroing the height to substrate, (**b**) plane fitting to terrace five and zeroing height to the lowest terrace, and (**c**) remeasuring a small portion with higher resolution, then again plane fitting to terrace five and zeroing height to the lowest terrace. Terraces are numbered consistently across the subfigures.

We then used two methods to measure the terrace heights and, therefore, the thickness of individual sheets (Supplementary Figure S35). First, a terrace profile (plotting the relative position along the selected axis versus the height at that position) was generated using Gwyddion. In this plot, terraces create flat portions which are fitted to linear trendlines, and the average height is obtained. In a second method, a histogram showing the height distribution was made. The vertex of peaks fitted on the histogram provided the mode height for each terrace. Both methods were used for the plane fitted images, while only terrace profiling was used for the unleveled image.

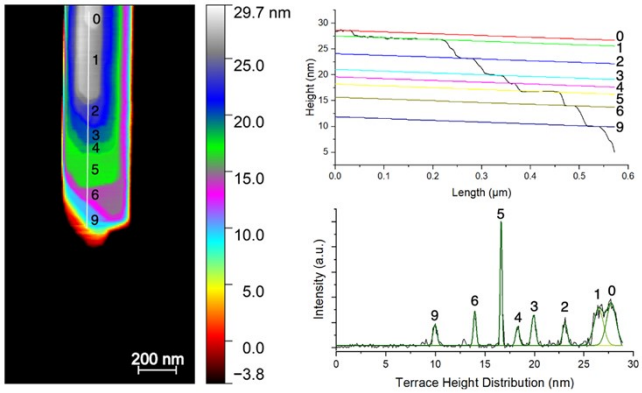

Supplementary Figure S35. Terrace profile (top) with linear trendlines assigned to terraces, and histogram (bottom) with peak fitting for the height analysis of the leveled and zeroed AFM image.

We used the step heights found in each of the five measurements (Supplementary Table S8) to determine the average sheet thickness. To determine the overall best fit sheet height h_{sheet}, we performed least squares regression analysis across all *n* step height data points. For each measured step of height h_{actual}, we assigned an estimated number of sheets *x* (1–3 sheets per step), which could be multiplied by a proposed sheet height h_{sheet}. The least squares analysis was then applied according to the following equation to find the sheet height h_{sheet}, which minimizes the error *r*:

$$r = \sqrt{\frac{\sum (h_{actual} - x h_{sheet})^2}{n}}$$

Based on this analysis, we selected the sheet height with the least error, 14.9 ± 4.5 Å, as the best fit. For the unmodified height and phase images used in Supplementary Figure S34, see Supplementary Figure S36.

Supplementary Table S8. All height data by terrace profiling and histogram peak fitting of the unleveled (purple), leveled (yellow), and higher resolution (red) AFM images, and their calculated step sizes h_{actual} and assigned no. of sheets *x* (green).

tag	Unleveled terrace height (nm)	Unleveled step size h_{actual} (nm)	Assigned no. of sheets *x*	Leveled terrace height (nm)	Leveled step size h_{actual} (nm)	Assigned no. of sheets *x*	Leveled histogram center (nm)	Leveled step size h_{actual} (nm)	Assigned no. of sheets *x*	High-res step size (nm)	High-res step size (nm)	Assigned no. of sheets *x*	High-res histogram center (nm)	High-res step size (nm)	Assigned no. of sheets *x*
0	--			27.79			27.76			--					
0.5	--	--	--	--	1.11	1	--	1.28	1	17.20	--	--	17.54	--	--
1	696.47			26.68			26.48			16.60	0.60	1	17.07	0.47	1
1.5	--	3.48	2	--	3.43	2	--	3.41	2	15.50	1.10	1	15.95	1.12	1
2	693.00			23.25			23.08			13.60	1.90	1	13.84	2.11	2
3	690.03	2.97	2	20.20	3.05	2	19.92	3.16	2	10.50	3.10	2	10.52	3.32	2
4	688.56	1.47	1	18.74	1.46	1	18.30	1.62	1	8.91	1.59	1	8.83	1.69	1
5	687.16	1.40	1	17.35	1.39	1	16.64	1.66	1	7.47	1.44	1	7.26	1.58	1
6	684.67	2.49	1	14.82	2.53	2	13.99	2.65	2	3.72	3.75	2	3.19	4.07	2
7	680.90	3.77	2	--	3.80	3	--	4.02	3	1.29	2.43	2	0.69	2.50	2
8	678.74	2.16	2	--			--			--	--	--	--	--	--
9	--	--	--	11.02			9.96			--	--	--	--	--	--

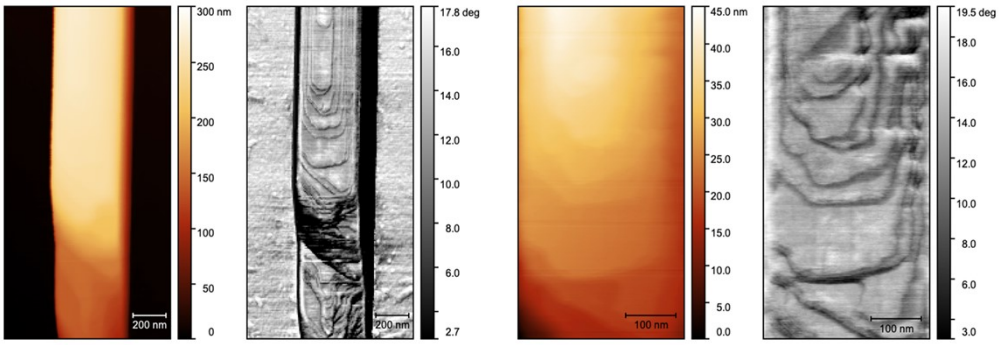

Supplementary Figure S36. Unmodified height and phase images used in Supplementary Figure S34.

To reinforce our sheet height analysis of Filament 1, we processed the AFM data from five additional exfoliated filaments of **H-N[5]HDI** (subfigures b–f in Supplementary Figure S37; subfigure a is Filament 1 from above). The raw image of each filament was plane fit to one of the terraces, then zeroed to the terrace height (as shown in Supplementary Figure S37).

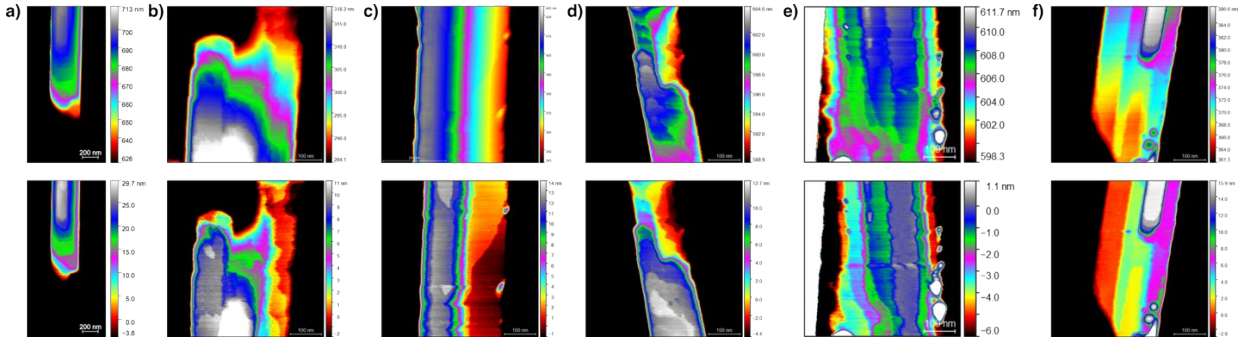

Supplementary Figure S37. AFM images of **H-N[5]HDI** filament terraces after exfoliation (top) and after processing by plane fitting and zeroing to terrace height (bottom) for six filaments (**a**–**f**).

We analyzed the sheet heights across the six filaments in two ways to ensure individual terraces could be identified (Supplementary Figure S38). First, a terrace profile (plotting the relative position along a drawn axis versus the height at that position) was generated using Gwyddion. In this plot, the flat portion of each terrace is selected, and the mean height of this selected region is obtained and used as the overall terrace height. In the second method, a histogram of the height distribution was generated, in which each terrace appears as a distinct cluster of counts. The mode of each cluster was taken as the height of that terrace. If a cluster was bimodal (e.g., Supplementary Figure S38d, terrace 9), the average of the two modes was used.

We used the step heights found in each of the terrace measurements (Supplementary Table S9) to determine the average sheet thickness. To determine the overall best fit sheet height h_{sheet}, we performed least squares regression analysis across all *n* step height data points. For each measured step of height h_{actual}, we assigned the estimated number of sheets *x* (1–3 sheets per step), which could be multiplied by a proposed sheet height h_{sheet}. The least squares analysis was then applied according to the following equation to find the sheet height h_{sheet}, which minimizes the error *r*:

$$r = \sqrt{\frac{\sum (h_{actual} - x h_{sheet})^2}{n}}$$

Based on this analysis, we selected sheet heights with the least error for each filament: 15.6±4.2 Å (Filament 1), 11.1±3.9 Å (Filament 2), 15.2±3.6 Å (Filament 3), 14.5±3.5 Å (Filament 4), 11.4±2.3 Å (Filament 5), and 15.4±5.0 Å (Filament 6).

Across all six filaments, the sheet height with the least error, 14.3±4.6 Å, was selected as the best overall fit.

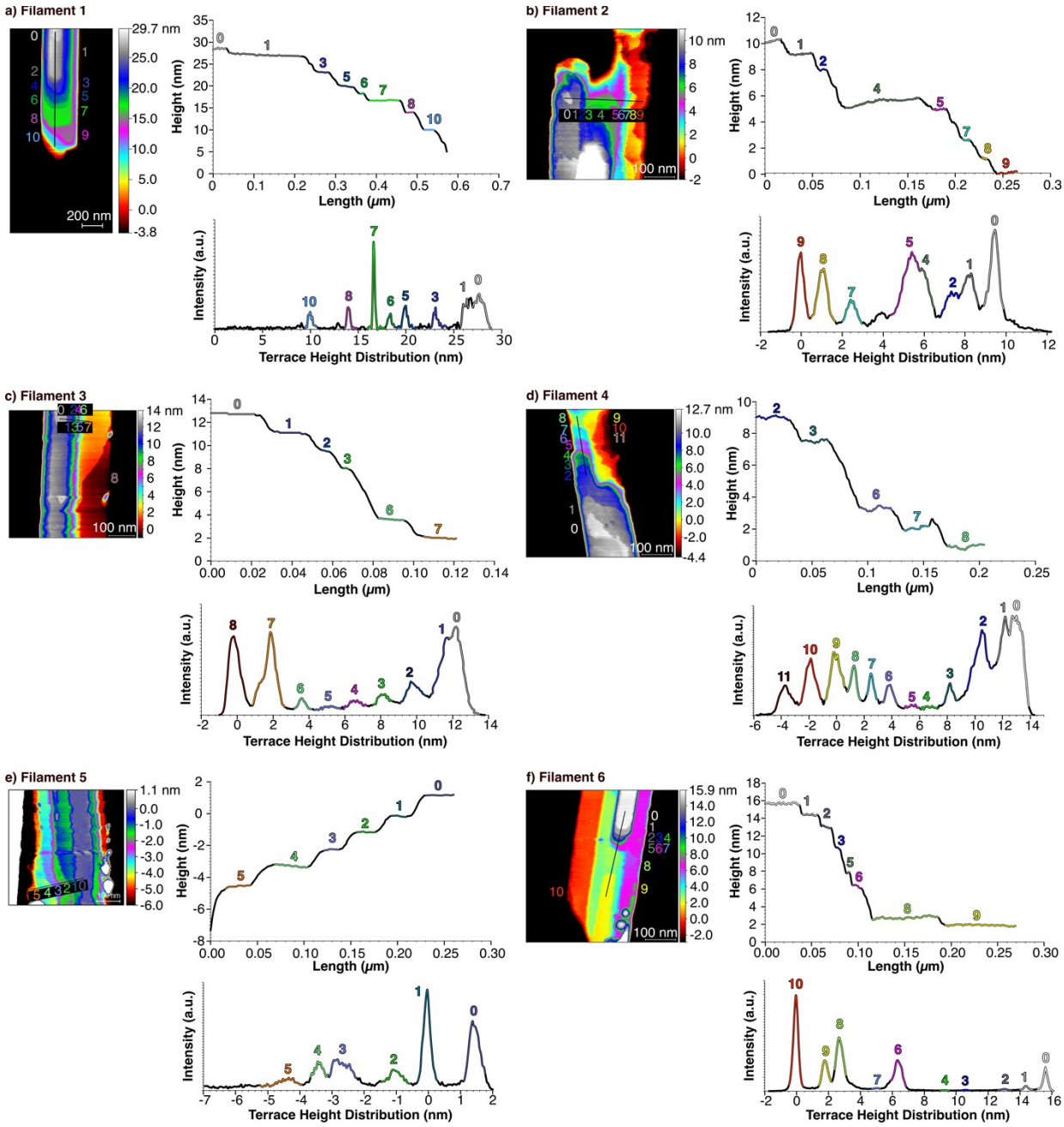

Supplementary Figure S38. For every subfigure (**a**–**f**), terrace profile (top graph) along the drawn axis (the black line in the AFM image), with the terrace regions used in the height analysis highlighted; and histogram (bottom graph) of the entire leveled and zeroed AFM image, with every highlighted peak corresponding to a terrace of the exfoliated filament.

Supplementary Table S9. All height data from terrace profiling and histogram peak analysis of the AFM images of the six filaments, and their calculated step sizes h_{actual}. Assigned no. of sheets $x = |tag_{top} - tag_{bottom}|$, where tag_{top} = the tag number for the top terrace of the measured step and tag_{bottom} = the tag number for the bottom terrace of the measured step.

	Filament 1				Filament 2				Filament 3			
tag	Profile height (nm)	Step size h_{actual} (nm)	Histogram height (nm)	Step size h_{actual} (nm)	Profile height (nm)	Step size h_{actual} (nm)	Histogram height (nm)	Step size h_{actual} (nm)	Profile height (nm)	Step size h_{actual} (nm)	Histogram height (nm)	Step size h_{actual} (nm)
0	28.53		27.70		10.09		9.47		12.74		12.20	
		1.44		1.30		1.00		1.18		1.64		0.50
1	27.09		26.40		9.09		8.29		11.10		11.70	
		3.93		3.30		1.20		0.97		1.57		2.04
2	--		--		7.89		7.32		9.53		9.66	
						2.45		1.45		1.52		1.64
3	23.16		23.10		--		--		8.01		8.02	
		3.24		3.10						4.40		1.34
4	--		--		5.44		5.87		--		6.68	
						0.57		0.48				1.49
5	19.92		20.00		4.87		5.39		--		5.19	
		1.63		1.60								1.57
6	18.29		18.40		--	2.34	--	2.98	3.61		3.62	
		1.56		1.80						1.60		1.79
7	16.73		16.60		2.53		2.41		2.01		1.83	
		2.74		2.70		1.41		1.31		--		2.01
8	14.00		13.90		1.12		1.10		--		-0.18	
		3.97		3.91		1.10		1.11		--		--
9	--		--		0.03		-0.01		--		--	
						--		--		--		--
10	10.03		9.99		--		--		--		--	
		--		--		--		--		--		--
11	--		--		--		--		--		--	

	Filament 4				Filament 5				Filament 6			
tag	Profile height (nm)	Step size h_{actual} (nm)	Histogram height (nm)	Step size h_{actual} (nm)	Profile height (nm)	Step size h_{actual} (nm)	Histogram height (nm)	Step size h_{actual} (nm)	Profile height (nm)	Step size h_{actual} (nm)	Histogram height (nm)	Step size h_{actual} (nm)
0	--		13.00		1.16		1.37		15.67		15.60	
		--		0.80		1.32		1.40		1.27		1.20
1	--		12.20		-0.16		-0.03		14.40		14.40	
		--		1.70		1.00		1.08		1.38		1.40
2	9.01		10.50		-1.16		-1.11		13.03		13.00	
		1.47		2.28		1.10		1.57		2.43		2.40
3	7.53		8.22		-2.27		-2.68		10.60		10.60	
				1.31		1.02		0.77				1.41
4	--		6.91		-3.28		-3.45		--	2.76	9.19	
		4.24		1.21		1.29		0.90				2.87
5	--		5.70		-4.57		-4.35		7.85		--	
				1.82		--		--		1.51		
6	3.29		3.88		--		--		6.33		6.32	
		1.23		1.41		--		--		3.58		1.25
7	2.06		2.47		--		--		--		5.07	
		1.16		1.21		--		--				2.42
8	0.90		1.26		--		--		2.75		2.65	
		--		1.46		--		--		0.85		0.90
9	--		-0.20		--		--		1.90		1.75	
		--		1.66		--		--		--		1.79
10	--		-1.86		--		--		--		-0.04	
		--		1.91		--		--		--		--
11	--		-3.77		--		--		--		--	

VII. Structure Elucidation Based on Wide-Angle X-ray Scattering

Two methods of sample preparation and scattering data acquisition were conducted to cross-validate the result and eliminate the influence of possible artifacts. A brief discussion is provided below.

By pipet, **H-N[5]HDI** ribbons were withdrawn from their mother liquor and drop-cast onto a Si wafer substrate for GIWAXS acquisition (see Supplementary Figure S49 for a picture of the drop-cast ribbons). A comparison of two-dimensional scattering patterns with the grazing angle varying among 0.12°, 0.3°, and 1° is shown in Supplementary Figure S39. In general, the data display a series of ring patterns corresponding to Bragg diffractions from microcrystalline domains of **H-N[5]HDI**. Scattering artifacts can be observed in addition to the ordered Bragg diffractions, including (1) anisotropic intensity due to preferred orientations of the microcrystalline fibers during the drop-casting process, matching the observed morphologies of **H-N[5]HDI** from optical images and SEM micrographs, (2) azimuthal angle-dependent peak shifts due to sample roughness, and (3) azimuthal angle-dependent peak shifts possibly due to strain-induced lattice distortion of the crystalline domains within the fibers, a result of combined factors of gravity, surface tension, and likely desolvation during the drop-casting and subsequent drying.

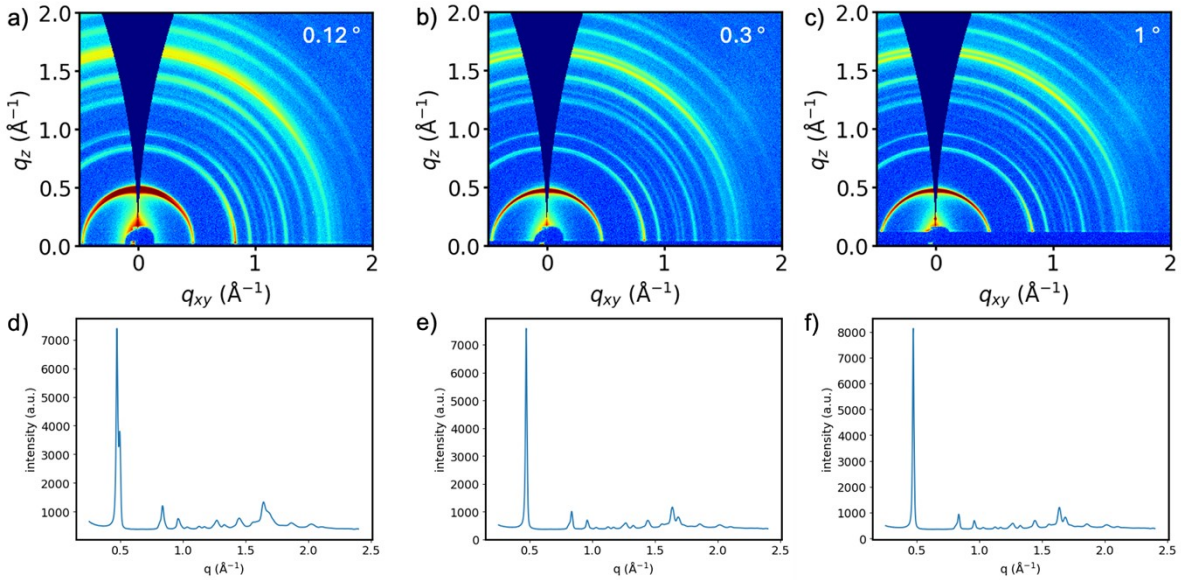

Supplementary Figure S39. Comparison of (**a—c**) two-dimensional and (**d—f**) integrated one-dimensional GIWAXS patterns of drop-cast **H-N[5]HDI** acquired at (**a,d**) 0.12°, (**b,e**) 0.3°, and (**c,f**) 1° grazing angles.

The integrated one-dimensional GIWAXS pattern with a grazing angle of 0.3° (Supplementary Figure S39e) was selected to preserve optimal data quality and minimize the influence from artifacts (1) and (2). To rule out artifact factor (3), an **H-N[5]HDI** ribbon from the mother liquor was packed in a 2 mm quartz capillary (wall thickness of 0.01 mm, Hampton Research), and its WAXS pattern was collected at BL11-3 in transmission mode. This preparation eliminates the drying and settling step compared to drop-casting on Si wafer. Integrated one-dimensional WAXS pattern obtained from this experiment is compared to the selected GIWAXS pattern in Supplementary Figure S40. The beam energy of incident X-ray for both GIWAXS and WAXS measurements is

12.7 keV. The sample to detector distance (290 mm) was corrected by a LaB_6 sample. In addition to Bragg diffractions attributable to **H-N[5]HDI** solids, a wide hump peaking at q ~ 1.5 $Å^{-1}$ corresponding to solvent scattering (DCM and EtOAc) can be observed. Compared to the GIWAXS data, no significant Bragg peak position discrepancy splitting was observed across the compared q range. The most contrast between the Bragg components of the WAXS and GIWAXS data were in peak width and intensity, which can be attributed to the different sample geometry and high X-ray absorption of the solvent. We thus conclude that the drying factor (3) has minimal influence on the data, and the 1D GIWAXS pattern with a grazing angle of 0.3° (Supplementary Figure S39e) will be used for following sections of structure elucidation.

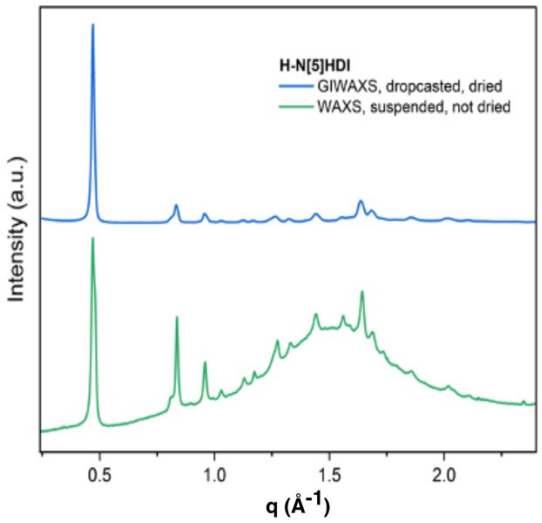

Supplementary Figure S40. Zoomed-in view of 1D GIWAXS pattern of **H-N[5]HDI** drop-cast on Si (top) and integrated 1D WAXS pattern obtained from an **H-N[5]HDI** ribbon packed in a quartz capillary (bottom).

In the following step, the integrated one-dimensional GIWAXS data (Supplementary Figure S39e) in q space was first converted to 2θ space assuming Cu Kα radiation (λ = 1.5406 Å), which was used for powder indexing in MDI Jade 6.5[9]. A set of unit cells selected by fitting merits and reasonability of cell volumes compared to calculated molecular volumes of **H-N[5]HDI** (performed using a geometrically-optimized model obtained using *Forcite* molecular mechanics optimization in *BIOVIA* Materials Studio 2020)[10] were used for modelling their atomic structure. For each unit cell, truncated **H-N[5]HDI** fragments (where 2-ethylhexyl side chains were replaced with methyl groups) were placed at different Wyckoff positions based on the symmetry of the space groups to populate the unit cell as an initial guess of structural solving. This tail truncation is based on the consideration that despite containing chiral centers, the 2-ethylhexyl groups are likely more disordered than the aromatic-diimide cores and, thus, likely contribute less to the X-ray diffraction. Powder solving was carried out using the *Reflex* module in *BIOVIA* Materials Studio 2020. The experimental pattern was first interpolated and background subtracted for solving. Each molecule was confined as a rigid group and structure solving using simulated annealing was performed. The resulting crystal structure was examined for structural conflict before re-adding the two 2-

ethylhexyl groups (one with an *R* stereocenter, the other with an *S* stereocenter) to the imides in the solution. This structure was further geometrically optimized using *Forcite* optimization before performing Pawley refinement in a 2*θ* (Cu Kα) range of 5–34° for fitting of the model to the experimental 1D data. Two structural models—one in space group *C*2 (Supplementary Table S10) and the other in space group *Cc* (Supplementary Table S11)—were found in best agreement with the data through Pawley refinement (Supplementary Figures S41 and S42). Notably, the *β* angles of both unit cells are in good agreement with the characteristic angles in **H-N[5]HDI** crystals observed in SEM micrographs (Supplementary Figure S8). Additionally, the bilayer sheet height ($= c \times sin(\beta)$) and monolayer sheet height ($= \frac{c \times sin(\beta)}{2}$) of both unit cells (26.7 Å/13.3 Å for both *C*2 and *Cc*) are in good agreement with the AFM measured sheet heights (Supplementary Information Section VI).

Supplementary Table S10. Fractional atomic coordinates of the structural model of **H-N[5]HDI** (*R,S* configuration) in *C*2 space group, resulting from the Pawley refinement against experimental GIWAXS data (from left-to-right: atom, x, y, z)

Monoclinic, *C*2
a = 10.1957 Å, *b* = 17.3403 Å, *c* = 32.4236 Å
α = *γ* = 90°, *β* = 124.6020°

C1	3.03379	0.26090	0.39473	**O31**	2.77229	-0.06311	0.12567	**H61**	1.47106	0.50552	1.31745
C2	2.97360	0.21277	0.35316	**C32**	5.03453	-0.06841	2.13032	**H62**	1.29235	0.45337	1.27763
C3	2.81855	0.22380	0.30902	**C33**	5.19016	-0.11685	2.15788	**H63**	1.50329	0.45627	1.39479
C4	2.71528	0.27680	0.31031	**C34**	5.17954	-0.17642	2.12073	**H64**	1.14829	0.50157	1.32138
C5	2.77808	0.32688	0.35141	**C35**	5.34449	-0.21069	2.13995	**H65**	1.30926	0.56527	1.33971
C6	2.93865	0.31902	0.39336	**H36**	4.92985	-0.10683	2.10845	**H66**	1.41976	0.55223	1.43032
C7	2.75378	0.18053	0.26445	**H37**	5.03327	-0.03235	2.10166	**H67**	1.26939	0.48349	1.41683
C8	2.58896	0.17705	0.22930	**H38**	5.29071	-0.07900	2.16702	**C68**	1.20499	0.62103	1.44352
C9	2.48460	0.22603	0.23090	**H39**	5.13170	-0.14947	2.08325	**C69**	1.17799	0.59682	1.39340
C10	2.54929	0.27885	0.27079	**H40**	5.09398	-0.22160	2.11447	**H70**	1.18784	0.57264	1.46194
N11	2.54743	0.12619	0.19263	**H41**	5.39687	-0.23780	2.17759	**H71**	1.11726	0.66553	1.43613
C12	2.68748	0.09985	0.20269	**H42**	5.42715	-0.16518	2.14448	**H72**	1.32845	0.64379	1.46972
C13	2.81891	0.13499	0.24453	**C43**	2.49943	-0.29708	1.11498	**H73**	1.19504	0.64633	1.37572
C14	2.97131	0.13058	0.25227	**C44**	2.33393	-0.26979	1.09906	**H74**	1.05226	0.57666	1.36737
C15	2.98864	0.07914	0.22131	**H45**	2.48597	-0.34359	1.08966	**C75**	1.43588	0.31941	1.40071
C16	2.85691	0.03547	0.18377	**H46**	2.56860	-0.31780	1.15474	**C76**	1.31113	0.37162	1.35861
C17	2.70323	0.04829	0.17308	**H47**	2.56727	-0.25056	1.11218	**H77**	1.53139	0.30530	1.39500
C18	3.09862	0.18035	0.28364	**H48**	2.26325	-0.31848	1.09806	**H78**	1.37666	0.26653	1.40018
C19	3.24543	0.17312	0.28938	**H49**	2.27067	-0.24564	1.06012	**H79**	1.49091	0.34635	1.43851
C20	3.26400	0.12049	0.26093	**C50**	2.39514	-0.13077	1.25029	**H80**	1.21387	0.37977	1.36451
C21	3.13386	0.07585	0.22503	**C51**	2.22992	-0.15376	1.20391	**H81**	1.25491	0.34257	1.32151
C22	2.44558	0.33609	0.27245	**H52**	2.49018	-0.14765	1.24492	**H82**	3.15493	0.25318	0.42818
N23	2.51100	0.38916	0.31102	**H53**	2.41871	-0.15815	1.28499	**H83**	3.04724	0.16621	0.35614
C24	2.67363	0.38722	0.34961	**H54**	2.40109	-0.06926	1.25628	**H84**	2.98919	0.35640	0.42574
C25	3.14277	0.03057	0.18776	**H55**	2.13816	-0.13898	1.21124	**H85**	2.35732	0.22452	0.20104
N26	3.02145	-0.01925	0.15560	**H56**	2.22680	-0.21582	1.20086	**H86**	2.43182	0.11350	0.16119
C27	2.88040	-0.01909	0.15333	**C57**	1.41164	0.45149	1.31482	**H87**	2.59773	0.02051	0.14161
O28	2.30167	0.33627	0.23891	**C58**	1.38483	0.44796	1.35801	**H88**	3.08478	0.22750	0.30175
O29	2.73358	0.43597	0.38231	**C59**	1.27602	0.51441	1.35182	**H89**	3.34400	0.21036	0.31458
O30	3.25678	0.03963	0.18481	**C60**	1.29402	0.53380	1.40170	**H90**	3.37819	0.11690	0.26541

Supplementary Table S11. Fractional atomic coordinates of the structural model of **H-N[5]HDI** (*R*,*S* configuration) in *Cc* space group, resulting from the Pawley refinement against experimental GIWAXS data (from left-to-right: atom, x, y, z)

Monoclinic, *Cc*
a = 10.3706 Å, *b* = 17.0396 Å, *c* = 32.8689 Å
α = *γ* = 90°, *β* = 125.7122°

C1	3.02998	0.26133	0.39661	**O31**	2.76881	-0.06321	0.13154	**H61**	1.46921	0.50634	1.29850
C2	2.96987	0.21311	0.35559	**C32**	5.02821	-0.06853	2.10742	**H62**	1.29073	0.45410	1.25886
C3	2.81501	0.22416	0.31178	**C33**	5.18365	-0.11704	2.13496	**H63**	1.50140	0.45701	1.37457
C4	2.71187	0.27725	0.31276	**C34**	5.17304	-0.17671	2.09842	**H64**	1.14685	0.50238	1.30142
C5	2.77459	0.32741	0.35331	**C35**	5.33778	-0.21104	2.11779	**H65**	1.30762	0.56620	1.31990
C6	2.93496	0.31954	0.39499	**H36**	4.92366	-0.10701	2.08564	**H66**	1.41798	0.55313	1.40923
C7	2.75032	0.18082	0.26781	**H37**	5.02695	-0.03240	2.07927	**H67**	1.26780	0.48427	1.39554
C8	2.58571	0.17734	0.23280	**H38**	5.28407	-0.07913	2.14422	**C68**	1.20348	0.62205	1.42158
C9	2.48148	0.22639	0.23407	**H39**	5.12525	-0.14971	2.06147	**C69**	1.17651	0.59779	1.37226
C10	2.54610	0.27930	0.27345	**H40**	5.08759	-0.22196	2.09203	**H70**	1.18634	0.57357	1.43961
N11	2.54422	0.12640	0.19666	**H41**	5.39009	-0.23818	2.15492	**H71**	1.11586	0.66661	1.41406
C12	2.68411	0.10002	0.20695	**H42**	5.42033	-0.16546	2.12247	**H72**	1.32678	0.64483	1.44767
C13	2.81537	0.13521	0.24844	**C43**	2.49629	-0.29756	1.10260	**H73**	1.19353	0.64739	1.35494
C14	2.96757	0.13080	0.25648	**C44**	2.33100	-0.27023	1.08649	**H74**	1.05093	0.57760	1.34633
C15	2.98488	0.07927	0.22612	**H45**	2.48286	-0.34415	1.07769	**C75**	1.43407	0.31993	1.38019
C16	2.85333	0.03553	0.18886	**H46**	2.56537	-0.31831	1.14186	**C76**	1.30948	0.37222	1.33847
C17	2.69984	0.04837	0.17790	**H47**	2.56405	-0.25096	1.10004	**H77**	1.52946	0.30580	1.37486
C18	3.09473	0.18064	0.28767	**H48**	2.26041	-0.31901	1.08529	**H78**	1.37493	0.26697	1.37950
C19	3.24136	0.17341	0.29374	**H49**	2.26782	-0.24604	1.04803	**H79**	1.48903	0.34692	1.41749
C20	3.25990	0.12069	0.26584	**C50**	2.39213	-0.13099	1.23522	**H80**	1.21235	0.38039	1.34398
C21	3.12993	0.07597	0.23020	**C51**	2.22712	-0.15400	1.18918	**H81**	1.25334	0.34313	1.30186
C22	2.44252	0.33664	0.27478	**H52**	2.48706	-0.14789	1.23022	**H82**	3.15097	0.25360	0.42983
N23	2.50785	0.38979	0.31286	**H53**	2.41567	-0.15840	1.26938	**H83**	3.04341	0.16649	0.35874
C24	2.67027	0.38784	0.35124	**H54**	2.39808	-0.06937	1.24113	**H84**	2.98544	0.35699	0.42695
C25	3.13883	0.03063	0.19361	**H55**	2.13548	-0.13921	1.19611	**H85**	2.35436	0.22489	0.20436
N26	3.01766	-0.01928	0.16166	**H56**	2.22400	-0.21617	1.18617	**H86**	2.42877	0.11369	0.16543
C27	2.87678	-0.01911	0.15902	**C57**	1.40986	0.45222	1.29574	**H87**	2.59447	0.02054	0.14669
O28	2.29878	0.33682	0.24141	**C58**	1.38309	0.44869	1.33810	**H88**	3.08091	0.22787	0.30543
O29	2.73015	0.43667	0.38354	**C59**	1.27442	0.51525	1.33170	**H89**	3.33981	0.21070	0.31878
O30	3.25269	0.03969	0.19105	**C60**	1.29240	0.53467	1.38075	**H90**	3.37394	0.11709	0.27059

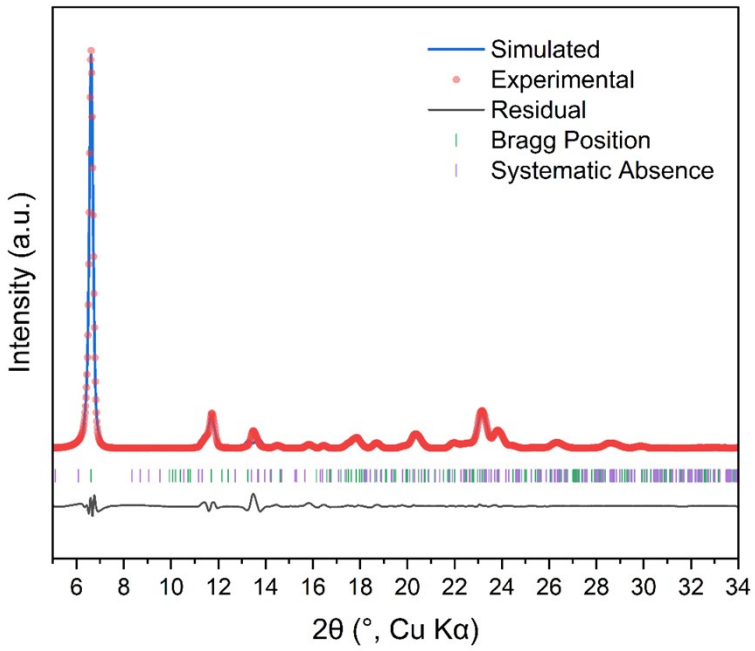

Supplementary Figure S41. Pawley refinement of **H-N[5]HDI** (*R*, *S* configuration) in *C*2 lattice (R_{wp} = 5.26%).

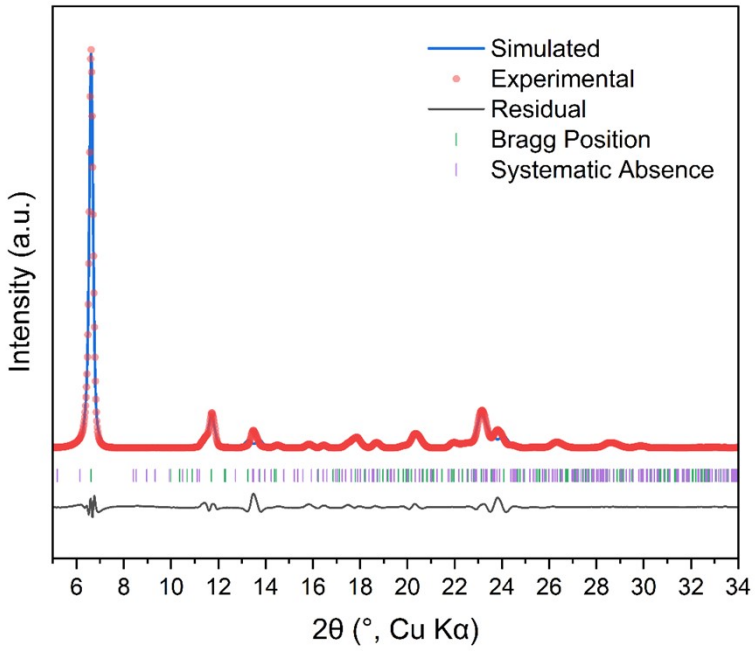

Supplementary Figure S42. Pawley refinement of **H-N[5]HDI** (*R*, *S* configuration) in *Cc* lattice (R_{wp} = 6.50%).

Lastly, phase contrast simulations of the *C*2 and *Cc* packing models of **H-N[5]HDI** were performed using the *ab*TEM package[11]. Both monoclinic cells were orthogonalized using the default *ab*TEM processing method. The simulated phase contrast of the *C*2 and *Cc* cells, along with the merged contrast from experimental high-resolution TEM micrographs, are shown in Supplementary Figure S43. Both simulated contrast maps show good agreement with the experimental merged map.

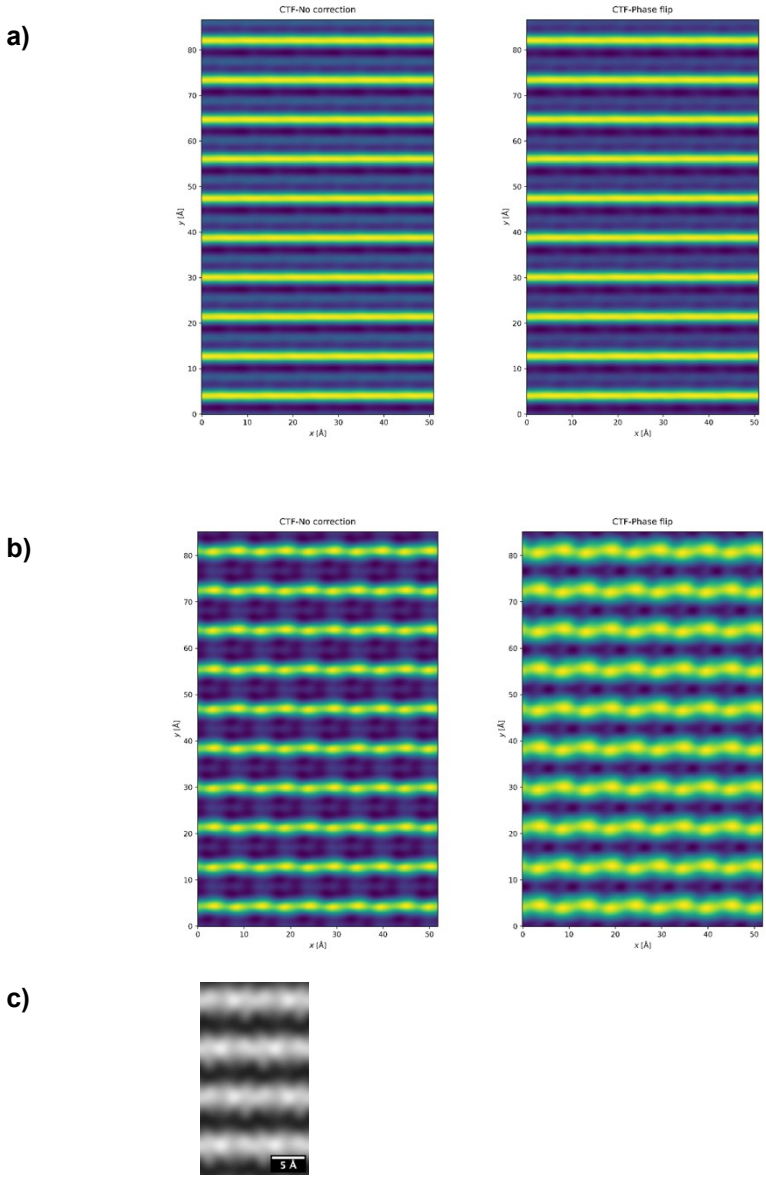

Supplementary Figure S43. Simulated phase contrast of the **H-N[5]HDI** structural model in (**a**) *C*2 space group and (**b**) *Cc* space group. (**c**) Merged phase contrast from the experimental high-resolution TEM micrograph of **H-N[5]HDI**. Additional details regarding the TEM analysis can be found in Supplementary Information Section VIII.

VIII. Cryogenic Transmission Electron Microscopy Imaging

Two conditions were used to prepare frozen hydrated and frozen dried specimens of **H-N[5]HDI**. A 3 µL droplet of ultrasonicated **H-N[5]HDI** ribbon was applied to a TEM copper grid and blotted using filter paper in a Vitrobot (FEI Company).

In the first condition, a copper TEM grid with a holey carbon film (300 mesh C-flat, Protochips, Inc.) was blotted for 4 seconds, then immediately plunged into liquid ethane to vitrify the specimen.

In the second condition, a molybdenum TEM grid with continuous carbon was used to reduce cryo crinkling and lattice deformation[12,13]. It was also blotted for 4 seconds and, after 30 seconds, then vitrified in liquid ethane.

The vitrified samples were stored and transferred to a 300 kV FEI Krios G2 for imaging under liquid nitrogen. Micrographs were collected using a Gatan K3 camera with an energy filter set at 20 eV slit width. The accumulated dose was 50 e/Å² per movie (10 frames), but only the first 6 frames (total dose of 30 e/Å²) were used for drift correction with MotionCorr2[14], resulting in motion corrected micrographs. Example micrographs are shown in Supplementary Figures S44 and S45.

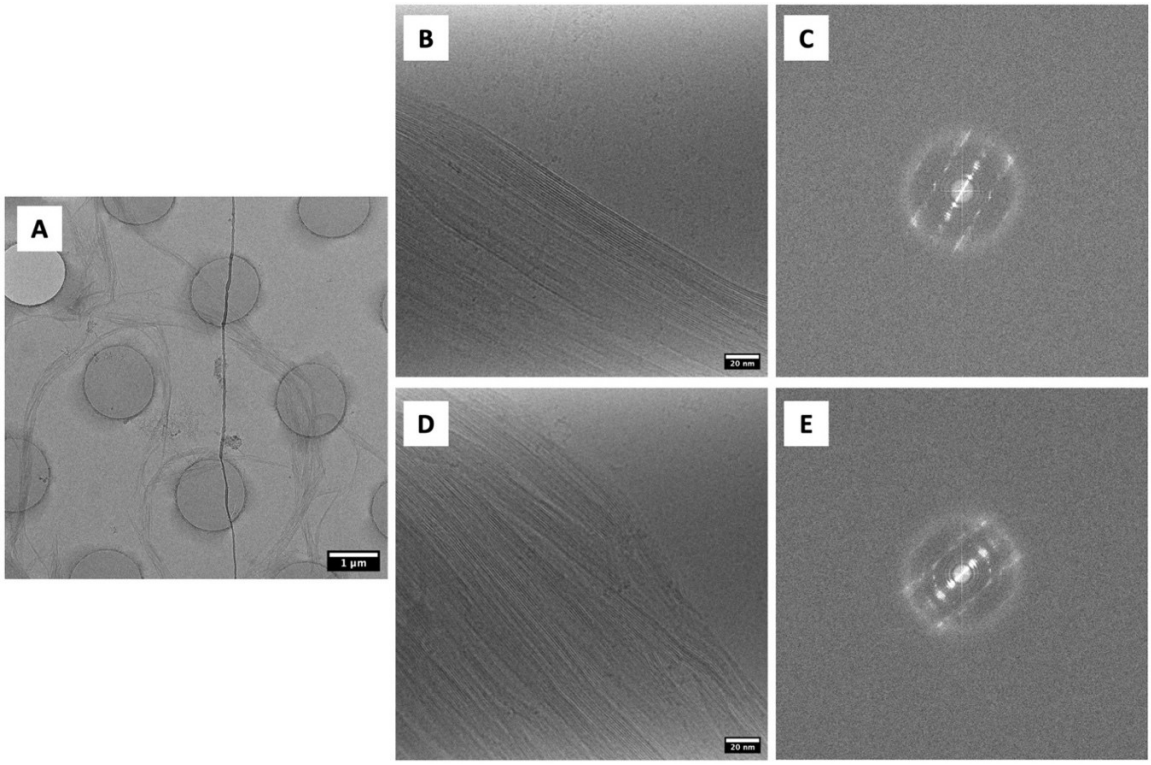

Supplementary Figure S44. Cryo-TEM micrographs and power spectra of frozen hydrated specimens. (**A**) A low magnification micrograph shows nanoribbons in vitreous ice within the holes. (**B**) A micrograph illustrates the morphology of a nanoribbon. (**C**) The corresponding power spectrum of **B** shows strong arc-shaped reflections due to the lack of long-range order in the crystalline ribbon, with a diffuse ring from the vitreous ice. (**D**,**E**) An additional example of nanoribbons in vitreous ice, showing identical lattice spacings.

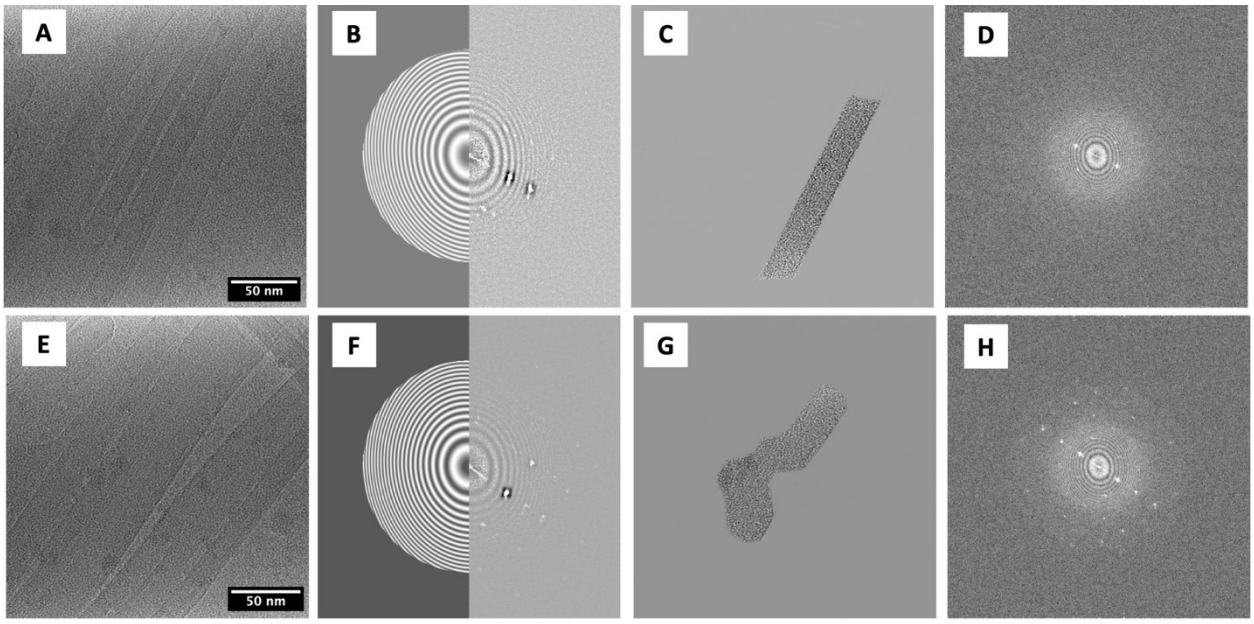

Supplementary Figure S45. Cryo-TEM micrographs and power spectra of frozen dried specimens for unbending and crystallography processing in Focus. (**A**) A micrograph shows the morphology of several nanoribbons. (**B**) A downsampled power spectrum from the micrograph in **A**, with the simulated CTF used for fitting on the left and the actual power spectrum on the right. (**C**) A mask was applied to the micrograph in **A** to extract a subregion with relatively long-range ordered lattices. (**D**) The power spectrum of the masked region. (**E**) Another micrograph shows the morphology of nanoribbons. (**F–H**). Analogous results to **B** and **C**, obtained from the micrograph in **E**.

Micrographs from the frozen dried specimens were processed for crystallography using the Focus software package[15]. A mask was applied to extract regions with short-range-ordered lattices due to the lack of long-range order, as shown in Supplementary Figure S45. Contrast transfer function (CTF) correction was performed using CTFFIND4[16], and lattice indexing and unbending were carried out in Focus.

Electrostatic potential maps were generated from individual micrographs (Supplementary Figure S46). Only reflections with good image quality (IQ < 6) from two micrographs were used for merging to obtain the final map shown in Supplementary Figure S47. The phase residual of merging reflections is 42.1^{o}, which is lower than 45^{o} [17].

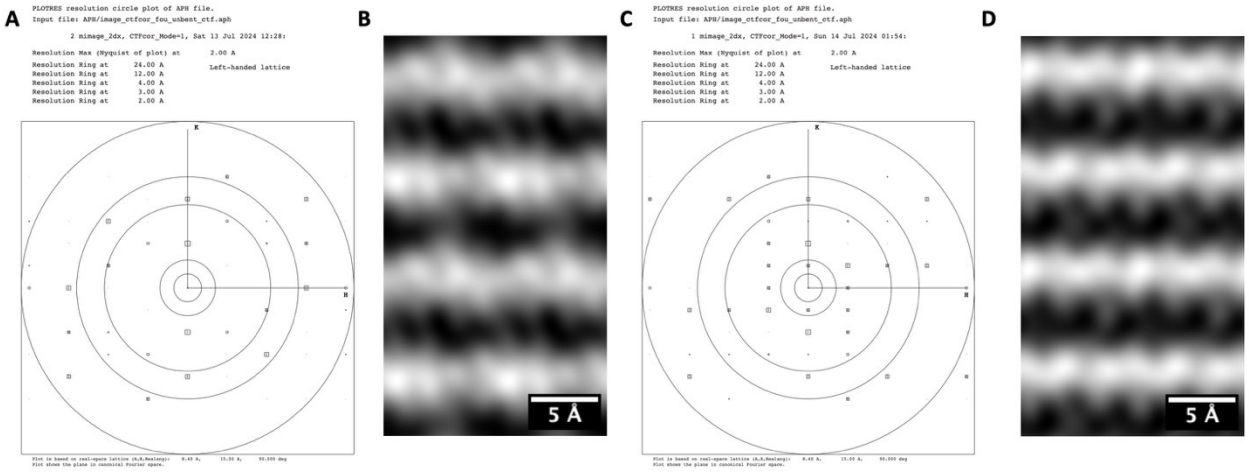

Supplementary Figure S46. Electrostatic potential and resolution maps of the crystals obtained using the two best micrographs from Supplementary Figure S45. (**A**) Conical resolution plots (with an outer ring up to 2 Å) and lattice reflections from Supplementary Figure S45C after the unbending process in Focus. (**B**) Electrostatic potential map showing the lattice structure in the crystal from Supplementary Figure S45C. The contrast is inverted compared to the micrograph, with bright regions representing electron dense molecules. (**C,D**) Analogous results to **A** and **B** obtained from the additional crystal in Supplementary Figure S45G.

A

PHASE RESIDUALS IN RESOLUTION RANGES

	DMIN	DMAX	IQ= 1	2	3	4	5	6	7	8	all IQs
1	1000.0	6.3	26.6	132.1	0.0	132.1	0.0	0.0	0.0	0.0	79.4
1			2	1	0	1	0	0	0	0	4
2	6.3	4.5	0.0	0.0	0.0	7.6	7.6	0.0	0.0	0.0	7.6
2			0	0	0	1	1	0	0	0	2
3	4.5	3.7	0.0	0.6	0.6	36.1	10.4	5.4	0.0	0.0	14.2
3			0	1	1	2	2	1	0	0	7
4	3.7	3.2	0.0	0.0	0.0	0.0	0.0	0.0	0.0	0.0	0.0
4			0	0	0	0	0	0	0	0	0
5	3.2	2.8	0.0	0.0	0.0	0.0	0.0	0.0	0.0	0.0	0.0
5			0	0	0	0	0	0	0	0	0
6	2.8	2.6	0.0	0.0	0.0	80.6	0.0	0.0	0.0	0.0	80.6
6			0	0	0	2	0	0	0	0	2
7	2.6	2.4	0.0	0.0	0.0	0.0	0.0	0.0	0.0	0.0	0.0
7			0	0	0	0	0	0	0	0	0
8	2.4	2.2	0.0	0.0	102.2	0.0	0.0	0.0	0.0	0.0	102.2
8			0	0	2	0	0	0	0	0	2
9	2.2	2.1	0.0	0.0	0.0	0.0	0.0	0.0	0.0	0.0	0.0
9			0	0	0	0	0	0	0	0	0
10	2.1	2.0	0.0	0.0	0.0	0.0	1.1	0.0	0.0	0.0	1.1
10			0	0	0	0	2	0	0	0	2
			26.6	66.4	68.4	62.2	6.1	5.4	0.0	0.0	
			2	2	3	6	5	1	0	0	

Overall: Phaseresidual = 42.112 Number of spots = 19

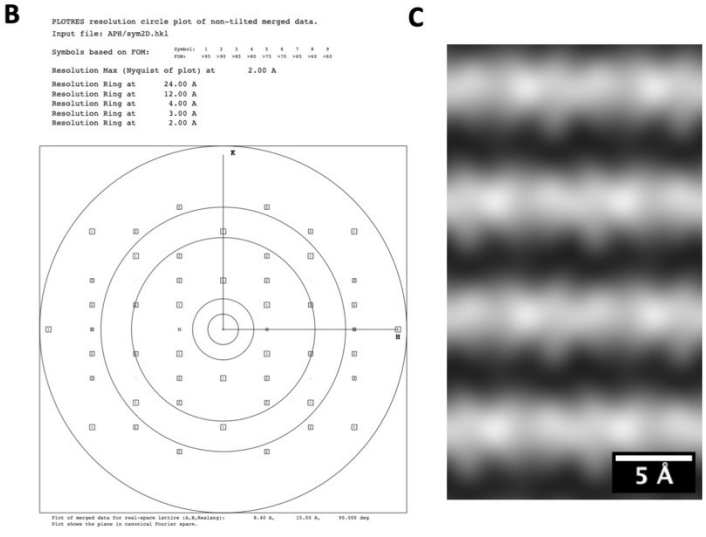

Supplementary Figure S47. Electrostatic potential and resolution maps after merging the two crystals from Supplementary Figure S45. (**A**) The table shows the phase residual after merging. (**B**) Conical resolution plots (with the outer ring up to 2 Å) and IQ of reflections after merging. (**C**) Electrostatic potential map showing the lattice structure in the merged crystal, with bright regions representing electron dense molecules.

IX. Additional Figures

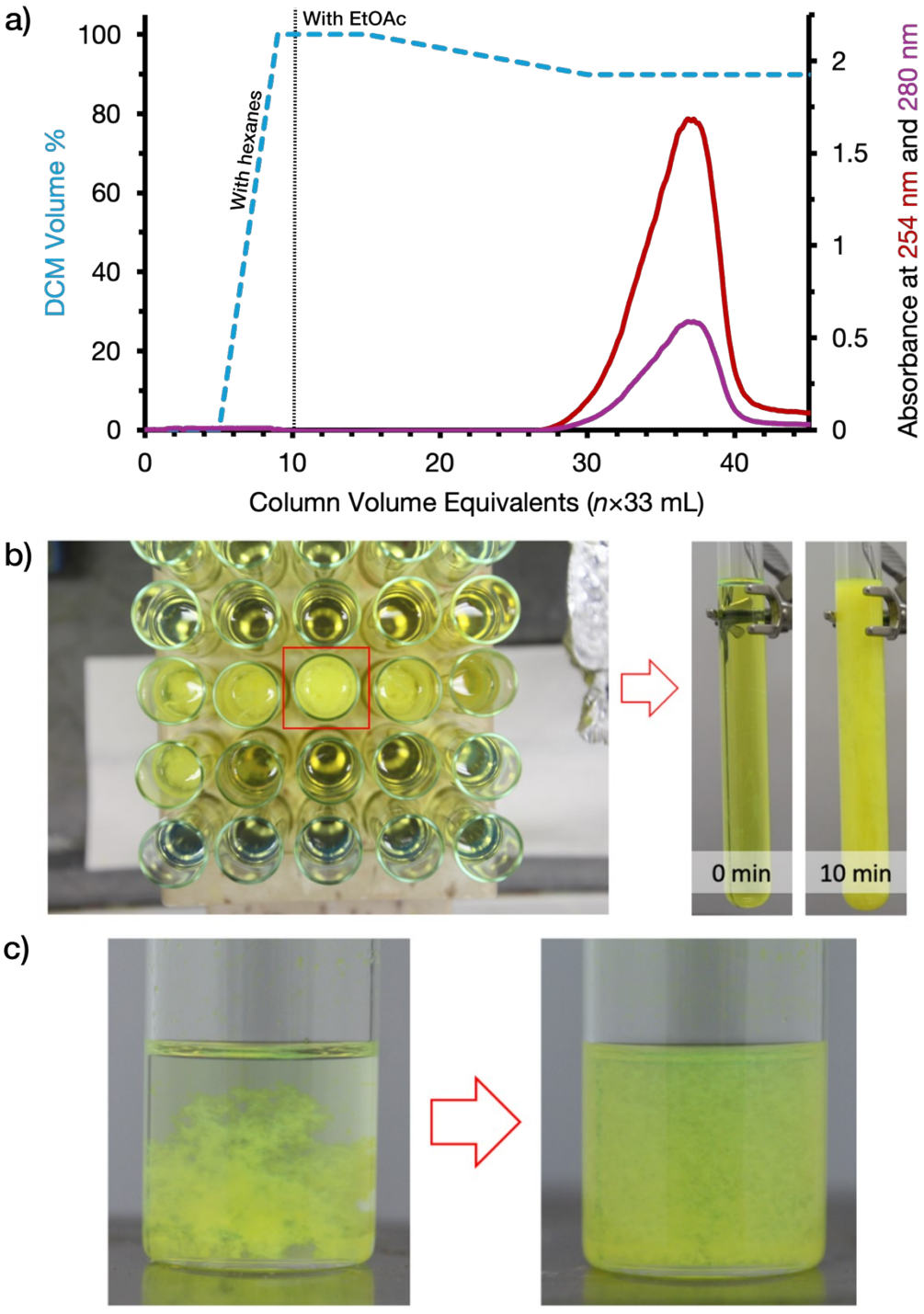

Supplementary Figure S48. (**a**) Auto-column traces of the collection of the ribbon growth solution of **H-N[5]HDI**, which eluted here from ~28-42 column volume equivalents (24-gram normal-phase silica flash column, flow rate of 35 mL min^{-1}). (**b**) The collected eluate of **H-N[5]HDI** (~25 mL per tube), the most concentrated of which grew ribbons rapidly. (**c**) In a 20-mL scintillation vial, 1 mL of concentrated ribbon liquor (9:1 DCM/EtOAc [v/v]) diluted in 9 mL of hexanes before (left) and after (right) ultrasonication.

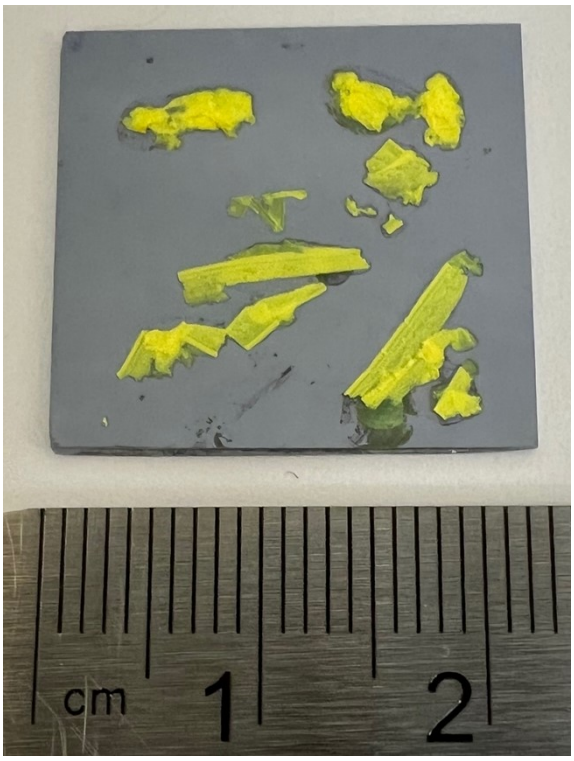

Supplementary Figure S49. Ribbons of **H-N[5]HDI** drop-cast by glass pipet onto a wafer of Si.

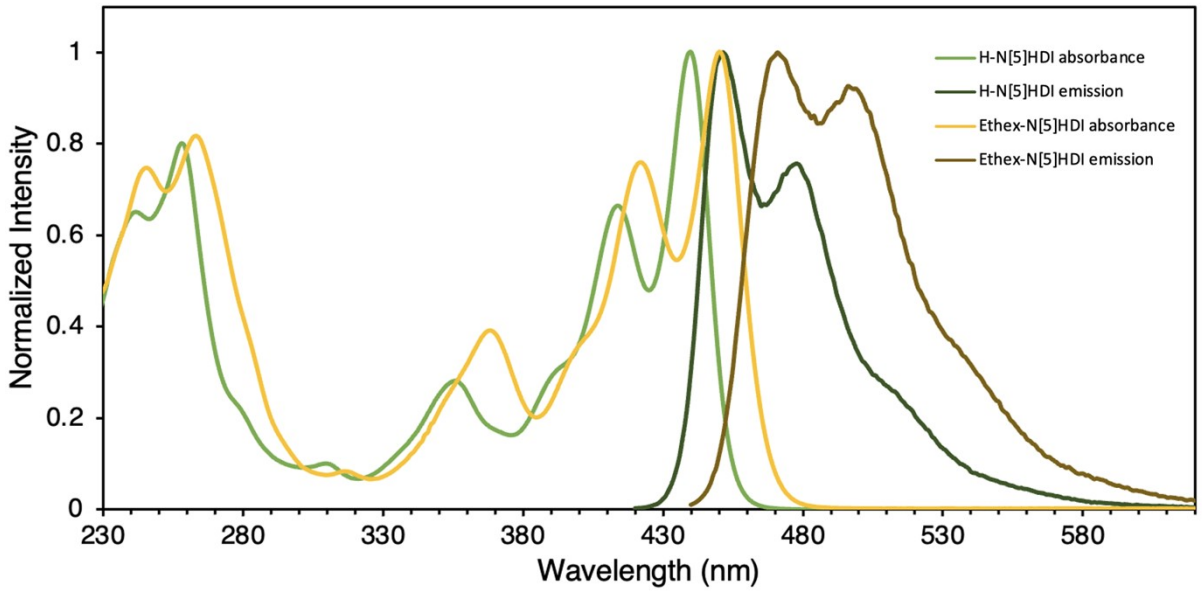

Supplementary Figure S50. UV-visible absorbance and fluorescence spectra of **H-N[5]HDI** (6.7 uM in DCM, excitation wavelength 410 nm) and **EtHex-N[5]HDI** (6.7 uM in DCM, excitation wavelength 430 nm). Quartz cuvette, 1-cm path length.

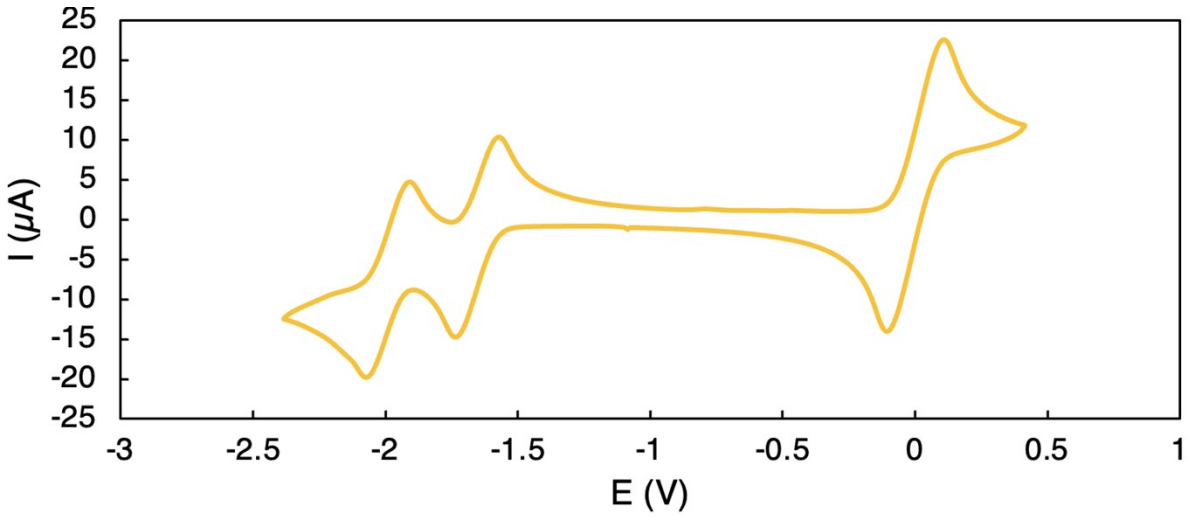

Supplementary Figure S51. Cyclic voltammogram (100 mV s^{-1} scan rate) of **EtHex-N[5]HDI** (1 mM) in degassed THF with 0.1 M $[Bu_4N][PF_6]$ as the supporting electrolyte. The potentials were referenced to a ferrocene/ferrocenium redox couple, whose half-wave potential is centered here at 0 V.

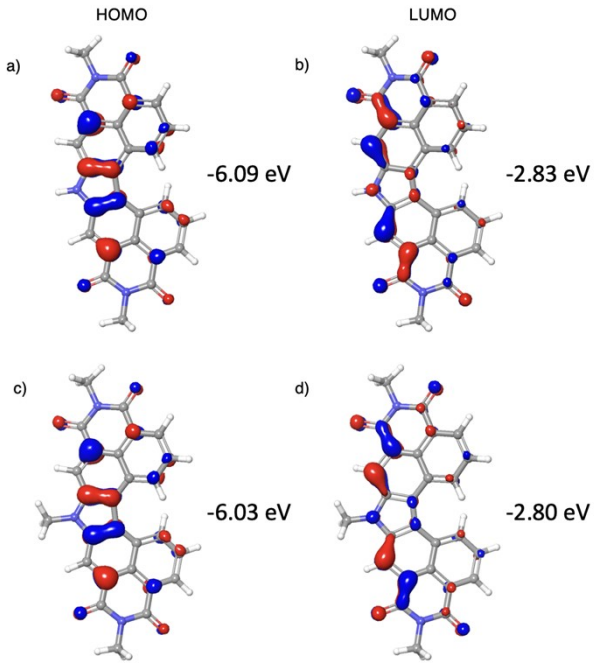

Supplementary Figure S52. The frontier molecular orbitals and their corresponding energies of the DFT-optimized structures of **H-N[5]HDI** and **EtHex-N[5]HDI** calculated at the B3LYP-D3/6-31G** level of theory. The HOMO (**a**) and LUMO (**b**) of **H-N[5]HDI**. The HOMO (**c**) and LUMO (**d**) of **EtHex-N[5]HDI**. The 2-ethylhexyl chains were truncated to methyl groups in these models to expedite the calculations. Molecular orbitals are rendered at 0.05 electrons $bohr^{-3}$.

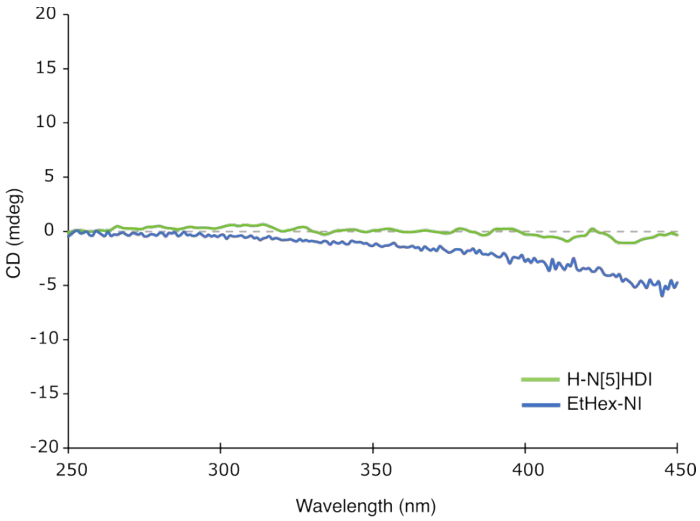

Supplementary Figure S53. CD spectra of solutions of **H-N[5]HDI** (10 μM in DCM) and **EtHex-NI** (10 μM in DCM). Both solutions were measured in a quartz cuvette with a 1-cm path length. The absence of CD confirms that the 2-ethylhexylamine used to prepare both **H-N[5]HDI** and **EtHex-NI** (a control compound with only one stereochemical element—the stereocenter on its 2-ethylhexyl chain; see Supplementary Information Section III for its structure) was racemic. The absence of CD also confirms that, in solution, for every stereoisomer of **H-N[5]HDI** there is an enantiomer of equal concentration.

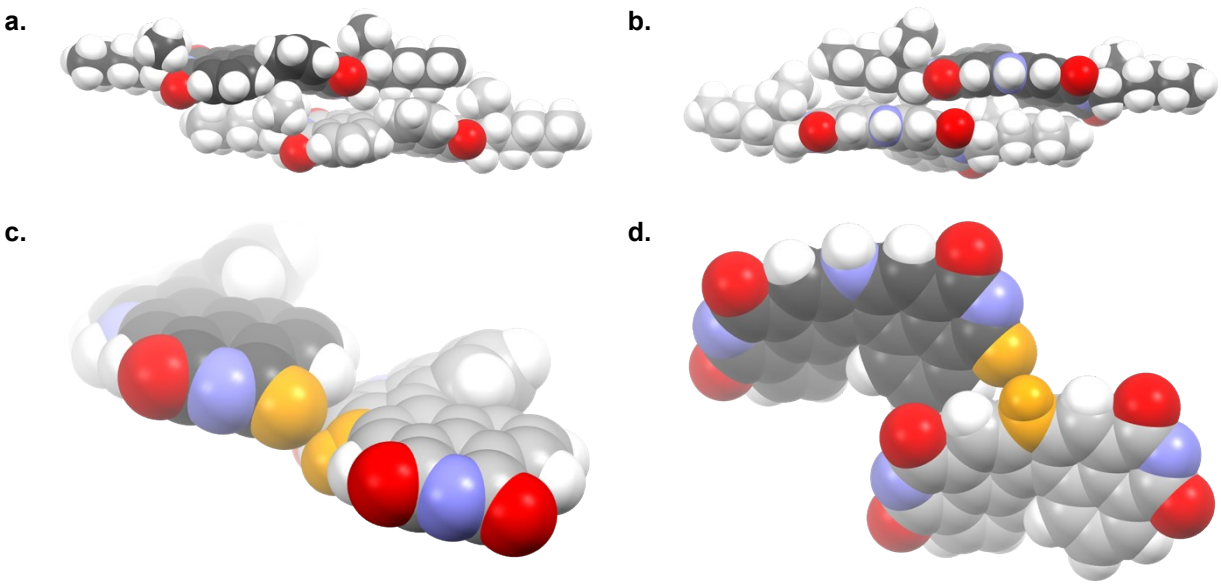

Supplementary Figure S54. (**a**,**b**) Different perspectives of the same dimer of **H-N[5]HDI** from the *C*2 packing model. These subfigures emphasize the extensive CH–π interactions between the alkyl chain of one molecule and the π-surface of the other. The same CH–π interactions are also present within the *Cc* packing model. (**c**,**d**) Different perspectives of the same dimer of **H-N[5]HDI** (not the dimer from subfigures **a** and **b**) from the *C*2 packing model, with alkyl chains hidden. These subfigures emphasize the weak hydrogen bond that links the molecular pair. Atoms participating in the hydrogen bond within this dimer (N–H···O) are highlighted in orange. The same weak hydrogen bonding is also present within the *Cc* packing model. In all subfigures (with the exception of the hydrogen bonding atoms highlighted in orange in **c** and **d**): O, red; N, blue; H, white; and C, grey (one molecule of **H-N[5]HDI**) or black (the other molecule of **H-N[5]HDI**).

X. Summary of Axially Chiral Molecules that Form Fibers

Helical Tecton	Were the fibers grown from an enantioenriched mixture?	Does the tecton have long, unbranched alkyl chains?	Did the helical tecton assemble into fibers in a weak solvent?	Reference (DOI)
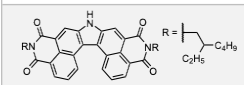	No, grown from a mixture of six stereoisomers.	No, *β*-branched chains.	No, dichloromethane and ethyl acetate.	*This work*
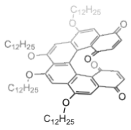	Yes, grown from enantiopure (−)-helicene. Racemic mixture does not form fibers.	Yes, unbranched *n*-dodecyl chains.	No, solid melt.	10.1021/ja973366t
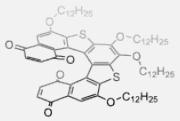	Yes, grown from enantiopure (*P*)-helicene. Racemic mixture does not form fibers.	Yes, unbranched *n*-dodecyl chains.	Yes, dodecane.	10.1021/ja011706b
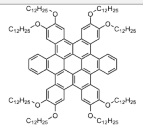	No.	Yes, unbranched *n*-dodecyl chains.	Yes, dodecane.	10.1021/ja0642360
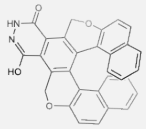	Yes, grown from enantiopure (*M*)-helicene. Racemic mixture forms short aggregates.	No alkyl chains.	No, chloroform and toluene.	10.1002/anie.201007849
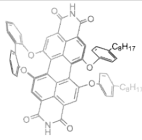	Yes, grown from enantiopure (*M*)- and (*P*)-isomer. Racemic mixture does not form fibers.	Yes, unbranched *n*-octyl chains.	Yes, methylcyclohexane.	10.1002/chem.201200089
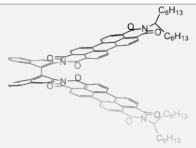	Yes, grown from enantiopure (*M*)- and (*P*)-isomer. Racemic mixture does not form fibers.	No, *α*-branched chains.	Yes, methylcyclohexane.	10.1002/anie.201500292
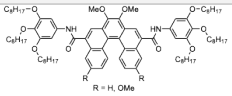	No.	Yes, unbranched *n*-octyl chains.	Yes, heptane.	10.1039/C5TC03675E
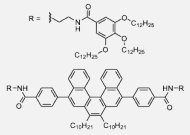	Yes, grown from enantiopure (*M*)-helicene. Racemic mixture does not form fibers.	Yes, unbranched *n*-dodecyl and *n*-decyl chains.	Yes, methylcyclohexane.	10.1021/acs.orglett.8b00565
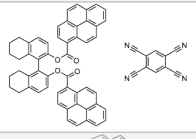	Yes, grown from enantiopure (*P*)-isomer.	No alkyl chains.	No, ethyl acetate and chloroform.	10.1002/anie.201902090
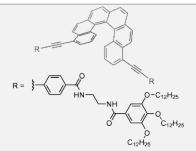	No, grown from racemic mixture and from enantiopure (*M*)- and (*P*)-helicene.	Yes, unbranched *n*-dodecyl chains.	Yes, methylcyclohexane.	10.1021/jacs.2c00556

XI. References

(1) Zhang, L. et al. Thio-bisnaphthalimides as Heavy-Atom-Free Photosensitizers with Efficient Singlet Oxygen Generation and Large Stokes Shifts: Synthesis and Properties. *Org. Lett.* **18**, 5664–5667 (2016).

(2) Babij, N. R. et al. NMR Chemical Shifts of Trace Impurities: Industrially Preferred Solvents Used in Process and Green Chemistry. *Org. Process Res. Dev.* **20**, 661–667 (2016).

(3) Budvari, S., O'Neill, M.J., Smith, A., & Heckelman, P.E. *The Merck Index, an Encyclopedia of Chemicals, Drugs, and Biologicals*, 11th ed. (Merck Co., Inc.,1989).

(4) Schneider, C. A., Rasband, W. S., & Eliceiri, K. W. NIH Image to ImageJ: 25 years of image analysis. *Nat. Methods* **9**, 671–675 (2012).

(5) Nečas, D. & Klapetek, P., Gwyddion: an open-source software for SPM data analysis, *Cent. Eur. J. Phys.* **10**, 181–188 (2012).

(6) Bochevarov, A. D., et al. Jaguar: A high-performance quantum chemistry software program with strengths in life and material sciences. *Int. J. Quantum Chem.* **113**, 2110–2142 (2013).

(7) Barroso, J. et al. Revisiting the racemization mechanism of helicenes. *Chem. Commun.* **54**, 188–191 (2018).

(8) Zhuang, B. et al. Influence of Charge Distribution on Structural Changes of Aromatic Imide Derivatives upon One-Electron Reduction Revealed by Time-Resolved Resonance Raman Spectroscopy during Pulse Radiolysis. *J. Phys. Chem. A* **122**, 8738–8744 (2018).

(9) JADE 6.5; Materials Data: Livermore, CA, 2002.

(10) BIOVIA, Dassault Systèmes, *BIOVIA* Materials Studio 2020, 20.1.0.2728, San Diego: Dassault Systèmes, 2019.

(11) Madsen, J. & Susi, T. The abTEM code:transmission electron microscopy from first principles [version 2; peer review: 2 approved]. *Open Res. Europe* **1**, 24 (2021).

(12) Booy, F. P. & Pawley, J. B. Cryo-crinkling: what happens to carbon-films on copper grids at low-temperature. *Ultramicroscopy* **48**, 273–280 (1993).

(13) Jiang, X., Xian, S., Zuckermann, R. N., Glaeser, R. M., Downing, K. H. & Balsara, N. P. Minimizing Crinkling of Soft Specimens Using Holey Gold Films on Molybdenum Grids for Cryogenic Electron Microscopy. *Microsc. Microanal.* **27**, 767–775 (2021).

(14) Zheng, S. Q., Palovcak, E., Armache, J.-P., Verba, K. A., Cheng, Y. & Agard, D. A. MotionCor2: anisotropic correction of beam-induced motion for improved cryo-electron microscopy. *Nat. Methods* **14**, 331–332 (2017).

(15) Gipson, B., Zeng, X., Zhang, Z. Y., & Stahlberg, H. *2dx*–User-friendly image processing for 2D crystals. *J. Struct. Biol.* **157**, 64–72 (2007).

(16) Rohou, A. & Grigorieff, N. CTFFIND4: Fast and accurate defocus estimation from electron micrographs. *J. Struct. Biol.* **192**, 216–221 (2015).

(17) Glaeser, R. M. *Electron crystallography of biological macromolecules*. (Oxford University Press, 2007).